Deep Neural Network-Based Inversion of Turbidites in Confined Basins

SEIYA FUJISHIMA[1] AND HAJIME NARUSE[1]

[1]Department of Geology and Mineralogy, Division of Earth and Planetary Sciences, Graduate School of Science, Kyoto University, Kyoto, Japan

Running title: DNN-BASED INVERSION OF TURBIDITES IN CONFINED BASINS

ABSTRACT

Turbidites generated by large earthquakes and other geological events are commonly preserved in small, topographically confined basins along active continental margins. Reconstructing flow conditions from these deposits is essential for assessing past hazards; however, existing inverse models have been validated only for unconfined settings, and their applicability to confined basins remains unclear. Here, we test a deep neural network (DNN)-based inverse framework using synthetic datasets generated in an idealized confined basin. Forward simulations reproduce key features of confined turbidity currents, including flow reflection and sediment ponding. Despite these complex dynamics, the trained DNN successfully reconstructs flow conditions with reasonable accuracy (SMAPE: 21.9–45.0%) using a limited number of training datasets. Notably, accurate inversion is achieved with as few as ten sampling points. These results demonstrate that inverse analysis of turbidites is feasible in confined basins even under sparse observational constraints. The proposed framework provides a practical basis for applying inverse modeling to natural deposits and offers a pathway toward linking turbidite records to the magnitude of their triggering events.

INTRODUCTION

This study proposes a novel inversion framework for reconstructing flow conditions of turbidity currents from their deposits (i.e., turbidites) in confined basins. Small scale (~10 km in diameter) submarine basins surrounded with topographic barriers are widely developed on submarine slopes in both passive and active tectonic settings, which are called confined basins or minibasin. In passive margins, salt-withdrawal minibasins along the Gulf Coast provide well-documented examples, typically only a few tens of kilometers in diameter with subsidence rates locally exceeding 10 km/My (Winker 1996; Prather 2000; Beaubouef et al. 2003a, 2003b; Hudec et al. 2009; Prather et al. 2012). In active margins, confined basins occur in trench and forearc slope settings. For example, along the Japan Trench, subduction of the Pacific Plate has produced trench- and graben-fill basins (Strasser et al. 2023), as well as smaller basins on the forearc slope (Arai et al. 2014; Ikehara et al. 2020).

Confined basins are typically filled with turbidites and hemipelagic mudstone, and their distinctive stratigraphic patterns have attracted attention in sedimentology and petroleum geology (e.g., Felletti 2002; Khan and Imran 2008; Kane et al. 2012; Wang et al. 2017). In such settings, turbidity currents interact with surrounding topographic highs, producing distinct sedimentary architectures that differ markedly from those in unconfined systems. In unconfined basins, characteristic elements of submarine-fan models, such as leveed channels and lobes, are commonly observed (Posamentier 2003; Posamentier and Walker 2006). In contrast, minibasins such as Basin IV of the Brazos–Trinity intraslope system in the Gulf Coast lacks leveed channels and instead exhibits distributary channel complexes resembling deltaic morphology (Beaubouef et al. 2003b).

The observed differences arise from the fundamental influence of basin confinement on turbidity current dynamics. Confined basins are enclosed entirely by topographic highs that trap incoming turbidity currents, forcing interactions between inflowing currents and those reflected from downstream barriers. These interactions generate hydraulic jumps and ponding, as demonstrated by flume experiments in which a turbidity current entering a slot-like confined basin produces an upstream-migrating bore (e.g., Lamb et al. 2004; Violet et al. 2005; Toniolo et al. 2006b; Spinewine et al.

2009). These processes can be reproduced by one-dimensional layer-averaged numerical model validated against experimental data (Toniolo et al. 2006a, 2006b).

Ponding has been suggested to produce distinctive topographic features within minibasins (Violet et al. 2005; Spinewine et al. 2009). In confined basins, turbidity currents are strongly decelerated by surrounding topographic barriers, causing the flow to become ponded within the basin interior. The ponded region acts as a temporary reservoir of fine-grained suspended sediment, leading to enhanced local deposition. More recent studies have highlighted the importance of three-dimensional flow structure in ponded regions. Horizontally two-dimensional flume experiments on minibasins exhibited that the reflected flows circulate along basin margins, generating large-scale eddies (Reece et al. 2024, 2025).

These distinctive depositional processes and stratigraphic architectures make confined basin deposits important for hydrocarbon exploration and natural hazard assessment. Rapidly subsiding minibasins can trap large volumes of sandy sediment (e.g., Gulf Coast, North Sea, Precaspian Basin; Hudec and Jackson 2007). Therefore, they can trap the vast quantities of continent-derived sediment, and deposits in minibasins are expected to be high-quality reservoir rocks (Jackson et al. 2020), making them favorable sites for hydrocarbon reservoir development.

Confined basins also play a key role in preserving event deposits related to geological hazards. Turbidites triggered by earthquakes, submarine landslides, and tsunamis are commonly accumulated in small, topographically confined basins along active margins (Goldfinger 2011). For example, along the Japan Trench, trench-axis basins contain turbidites correlated with major megathrust earthquakes (Ikehara et al. 2020, 2021; Strasser et al. 2023, 2024; Pizer et al. 2025), and their spatial distribution has been used to infer past rupture extent (Strasser et al. 2024). Similar observations from the Cascadia subduction zone further indicate that isolated confined basins enable clear stratigraphic correlation of seismogenic turbidites (Goldfinger et al. 2017). These examples highlight that confined basins can preserve event deposits with high fidelity, providing valuable records of past geological hazards.

Despite their importance, the potential of confined-basin turbidites to quantitatively constrain flow conditions and triggering events remains largely unrealized. In principle, deposits accumulated within confined basins should provide valuable information on the magnitude and dynamics of turbidity currents, as well as the scale of the triggering events. Such information would be particularly useful for reconstructing flow behavior in areas where direct observations are lacking. However, no attempts have been applied to estimate quantitative flow parameters from confined basin deposits. This gap highlights a critical need for robust inversion frameworks capable of linking deposit characteristics to flow conditions in confined-basin settings.

Traditionally, the flow conditions of turbidity currents have been estimated from turbidites using deposit grain size as a proxy (e.g., Bowen et al. 1984; Komar 1985; Hiscott 1994), but mathematical optimization has led to significant advances in the inversion of turbidity currents. A one-dimensional inverse model based on a deep neural network (DNN) was proposed by Naruse and Nakao (2021) and demonstrated reasonable performance against experimental data (Cai and Naruse 2021). This DNN-based inverse model has been extended to two horizontal dimensions and successfully applied to estimate flow conditions of experimental turbidity currents at unconfined basins (Fujishima and Naruse 2026). However, this DNN-based inverse model has not yet been tested in confined basins, where turbidity currents are expected to exhibit complex flow behaviors.

Therefore, this study aims to develop a horizontally two-dimensional DNN-based inverse model for turbidites in confined basins and to evaluate its performance. First, forward simulations were conducted to examine the sensitivity of the calculation results to the input parameters and to investigate the complex behavior of turbidity currents in confined basins. Second, inverse models were trained using various numbers of training datasets generated by the forward model. Finally, the performance of the trained inverse models was evaluated with respect to the number of training datasets, the number of sampling points, and the presence of noise in the input data.

FORWARD MODEL

Numerical model of turbidity currents

We employ a horizontally two-dimensional layer-averaged model as a forward model of turbidity currents to produce training datasets for the DNN-based inverse model. The forward model is based on the four-equation model proposed by Parker et al. (1986), which consists of fluid mass, fluid momentum, suspended sediment mass, and turbulent kinetic energy conservation (see Appendix A for details). In this study, the original four-equation model was extended to two horizontal dimensions to represent the spreading and reflection of turbidity currents within a confined basin. To account for the settling interface of current due to particle settling, water detrainment is incorporated following Toniolo et al. (2006a).

Numerical Experiments of Ponded Turbidity Currents

Numerical simulations were conducted to investigate the dynamics of turbidity currents and the resulting turbidite characteristics in the confined basin. The calculations were conducted using the inlet conditions of flow velocity $U_0 = 2\ \mathrm{m/s}$, suspended sediment concentrations $C_{0,1} = C_{0,2} = 0.0025$, for particle diameters $D_{\mathrm{s1}} = 20\ \mu\mathrm{m}$ and $D_{\mathrm{s2}} = 3\ \mu\mathrm{m}$, respectively, flow thickness $h_0 = 10$ m, and flow duration $T_d = 432{,}000$ s. The initial topography and other parameters were set to the same values as those used in the generation of training datasets described below. After the calculation, spatial and temporal variations of flow behavior and deposit features were observed.

Sensitivity Test

A sensitivity analysis was conducted to evaluate how the inlet parameters influence the results of forward simulations in the confined basin. Five cases were examined (Table 1): a baseline case (Case 1) and four additional cases (Cases 2–5) in each of which one of the inlet parameters ($C_{0,i}$, U_0, h_0, or T_{d}) was doubled relative to the baseline. Except for the modified parameter, the initial topography and all other calculation conditions were identical to those used to generate the training datasets. Differences in the resulting spatial patterns of deposit thickness were then compared among the cases.

INVERSE MODEL

DNN-Based Inverse Model

The DNN-based inverse models were developed to estimate the input parameters of the forward model from the deposits. The model architecture was based on that used in Fujishima and Naruse (2026). The training datasets were generated using the forward model, and the inverse model learned the relationship between sediment volume per unit area at sampling points and the forward-model input parameters from these datasets. This training enables the inverse model to estimate the input parameters from the sediment volume per unit area (Fig. 1; see Appendix B for details). The trained model was evaluated using independent datasets that were not used for training (Fig. 1). The conditions for generating the training datasets, the training conditions for the inverse model, and the evaluation of its performance are described below.

Generation of Training Datasets

Numerical simulations were conducted in an idealized confined basin to generate synthetic deposits for training the inverse models (Fig. 2). The computational domain was 19 km long in the streamwise direction and 8 km in the lateral direction. The upstream slope was set to 2%, leading into a flat basin floor with a length of 12 km and a width of 4 km. On both sides of the basin floor, lateral basin slopes with a gradient of 10% and a width of 2 km were prescribed. At the downstream end, a topographic barrier was imposed, consisting of a 10% slope with a length and width of 2 km. The inlet at the upstream boundary had a width of 1 km. The grid spacing Δx was set to 100 m in both the streamwise and lateral directions.

At the upstream boundary, the depth-averaged flow velocity, flow thickness, and suspended sediment concentration were specified as constant values during the flow duration T_d (Dirichlet boundary condition). Zero-gradient boundary conditions (Neumann boundary conditions) were applied at the downstream and lateral boundaries.

The inlet conditions were defined by the depth-averaged velocity U_0, flow thickness h_0, suspended sediment concentration for each grain-size class $C_{0,i}$, and the flow duration T_{d}. A continuous turbidity current was assumed such that inlet conditions were held constant over T_{d}. Two grain-size classes were used, with particle diameters $D_{\mathrm{s},1} = 20\ \mu\mathrm{m}$ and $D_{\mathrm{s},2} = 3\ \mu\mathrm{m}$. The values of U_0, h_0, $C_{0,i}$, and T_{d} were randomly sampled from uniform distributions within the ranges listed in Table 2. Each sampled parameter set was used to perform a forward simulation, and the resulting deposits were stored as elements of the training datasets.

Training Conditions of DNN-Based Inverse Model

The inverse models were trained with varying numbers of training datasets, ranging from 500 to 14,500 in increments of 500, to evaluate the effect of training data size on inversion performance. The model parameters (weights and biases) corresponding to the epoch with the lowest validation loss were selected and used for subsequent analyses, including the evaluation of the inverse model performance and the investigation of the effect of sampling point density on inverse model performance. The corresponding model training required several hours to approximately one day, depending on the number of training datasets, with an Intel Core i7-13700KF and an NVIDIA GeForce RTX 4060.

Evaluation of Inverse Model Performance

The performance of the trained inverse models was evaluated using synthetic test datasets. A total of 100 test datasets were generated independently of the training datasets. The input parameters were sampled from the same uniform distributions and ranges as those used for the training datasets (Table 2), and forward calculations were performed. In this way, 100 pairs of deposit thickness values at the same sampling points as those used for the training datasets, along with their corresponding input parameters, were generated and these pairs were used as the test datasets. The deposit thickness values were then input into the inverse model, and the errors between the estimated and true input parameter values were calculated. No additional procedure was applied to exclude parameter combinations that were identical to those in the training datasets, as the probability of such an occurrence was negligibly small.

The errors between the estimated and true input parameters were then calculated using the root-mean-square error (RMSE), bias (b), and symmetric mean absolute percentage error (SMAPE) as evaluation metrics. The definitions of RMSE, b, SMAPE are as follows:

$$\mathrm{RMSE} = \sqrt{\frac{1}{N}\sum_{n}\left(y_{\mathrm{pn}} - y_n\right)^2}, \tag{21}$$

$$b = \frac{1}{N}\sum_{n}\left(y_{\mathrm{pn}} - y_n\right), \tag{22}$$

$$\mathrm{SMAPE} = \frac{100}{N}\sum_{n}\frac{2\left|y_n - y_{\mathrm{pn}}\right|}{\left|y_n\right| + \left|y_{\mathrm{pn}}\right|}, \tag{23}$$

where N is the number of test datasets. The variables y_n and y_{pn} denote the true and predicted values of a parameter in the nth test dataset, respectively.

Effect of Sampling Point Density on Inverse Model Performance

The performance of the inverse model was also evaluated as a function of sampling-point density. In natural outcrops, it is often difficult to obtain laterally continuous two-dimensional measurements of turbidite thickness or grain-size distributions. Therefore, understanding how inversion accuracy depends on the number and location of sampling points is essential for practical applications.

To assess the effect of the sampling point configuration on the inverse analysis, inverse analyses were performed using the following sampling point configurations. The effect of the number of sampling points in the longitudinal direction was then examined by distributing the sampling points from upstream to downstream and increasing their number from 10 to 70 in increments of 10 (Fig. 3). Next, the effect of lateral distribution was examined using a base configuration of 10 points distributed longitudinally from upstream to downstream. Additional sampling points were added in the lateral direction in increments of 10, resulting in configurations with 20, 30, 40, and 50 points (Fig. 4). For each configuration, an inverse analysis was performed, and the resulting loss function value was used to evaluate the effect of the sampling point configuration.

Robustness against Observation Errors

The robustness of the inverse model to observational uncertainties was also evaluated. The inversion framework in this study requires bed thickness and grain-size distributions as input; however, both measurements inevitably contain observational noise arising from coring, outcrop logging, and laboratory analyses. To assess how such uncertainties affect inversion accuracy, artificial noise was added to the test datasets, and the resulting discrepancies between the predicted and true inlet parameters were quantified.

Noise was introduced by multiplying the noise-free test data, x_{test}, by random perturbations drawn from a standard normal distribution, scaled by a noise ratio, r. Values of r ranging from 0.01 to 0.2, with increments of 0.01, were generated, corresponding to noise levels from 1% to 20% of the original data. Noisy test data, $x_{\mathrm{test,\,noise}}$, were generated as:

$$x_{\text{test, noise}} = x_{\text{test}} + r\epsilon \odot x_{\text{test}}, \tag{24}$$

where the element-wise product (Hadamard product) is denoted by $\odot$, and ϵ is a vector of random values sampled from a standard normal distribution.

The inversion was performed for each r, and the SMAPE between predicted and true input parameters of the forward model was computed. For each r, random noise ϵ was independently generated ten times to create ten noisy test datasets according to Equation 24. The inverse model was then applied to each noisy dataset, and the SMAPE value was calculated. The mean SMAPE over ten independent trials was used as a measure of the robustness of the inverse model to observational noise. The mean SMAPE value was calculated as:

$$\text{Mean SMAPE} = \frac{1}{M}\sum_{m}\frac{100}{N}\sum_{n}\frac{2\left|y_{mn} - y_{\text{p}mn}\right|}{\left|y_{mn}\right| + \left|y_{\text{p}mn}\right|}, \tag{25}$$

where M is the number of input parameters of the forward model, y_{mn} is the true value of the nth test dataset in the mth parameter, and $y_{\text{p}mn}$ is the corresponding predicted value.

The inverse model for unconfined basins developed by Fujishima and Naruse (2026) was also evaluated for robustness against noisy input data, and its performance was compared with that of the present study. For this comparison, the inverse model for Run 1 of Series 1 was adopted. The inversion was performed on the test datasets from the previous study with the same range of r as described above, and the mean SMAPE was calculated. The results were then compared with those of the inverse model for a confined basin developed in this study.

RESULTS

Flow Dynamics and Depositional Patterns in Confined Basin

The example of the forward simulation exhibited that the turbidity currents in the confined basin developed complex eddies. The inflowing turbidity current reached the downstream barrier and was reflected at approximately 20,000 seconds after the start of the experiment (Fig. 5A). Following the reflection, a bore propagated upstream (Fig. 5B), and the hydraulic jump formed at the boundary between the bore and the inflowing current. The location of hydraulic jump became stabilized near the upstream slope break by approximately 50,000 seconds (Fig. 5C). Eddies were generated at the location of the hydraulic jump and subsequently spread throughout the basin (Fig. 5D, E, F).

The ponded turbidity current with large-scale eddies formed a distributary channel on the basin floor. Initially, a single channel developed and migrated downstream, where flow state was Froude-supercritical at around 100,000 seconds after the start of the experiment (Fig. 6A, B). As the eddies developed and migrated downstream, the Froude-supercritical region shifted laterally (Fig. 6C, E), resulting in the channel migration and branching. The channel progressively widened, accompanied by a decrease in channel depth (Fig. 6D, F).

Sensitivity of Forward Model to Inlet Parameters

Sensitivity tests of the forward model demonstrated that deposit thickness in the confined basin was strongly influenced by the flow velocity at the inlet and flow duration. In the baseline case (Case 1), the flow eroded the upstream slope and formed a channel-like topography on the basin floor (Fig. 7A). In Case 5, where the flow duration was doubled, the flow produced sinuous channel-like topography on the basin floor, and the deposit thickness outside the channelized feature was approximately twice that in Case 1 (Fig. 7E). The calculation doubled the flow velocity (Case 3) generated a channel-like topography with a wider channel than that of Case 1 (Fig. 7C). The suspended sediment concentration at the inlet also affected on the distribution of bed thickness, but its influence was less pronounced than that of flow velocity and duration. The case with doubled suspended sediment concentration (Case 2) produced a channel-like topography that was similar to that of Case 1, but the bed thickness was approximately doubled (Fig. 7B).

In contrast, flow thickness had a comparatively minor effect on the deposit distribution. In Case 4, where h_0 was doubled, the resulting channel was slightly wider than in Case 1, but overall spatial patterns more closely resembled the Case 1 than Cases 3 or 5 (Fig. 7D).

Effect of Number of Training Datasets

The inverse model achieved satisfactory performance with a relatively small number of samples, but notable improvements were observed up to approximately 6,000 training datasets. As the number of training datasets increased, the minimum training loss decreased monotonically; however, the change was relatively small (Fig. 6). Similar to the training loss, the minimum validation loss decreased substantially as the number of training datasets increased from 500 to 6,000 and then exhibited little change beyond 6,000 datasets. These results indicate that approximately 6,000 training datasets are sufficient to achieve stable inversion performance, with little additional benefit from larger datasets. Accordingly, the inverse model used in the following analyses was trained on 6,000 datasets.

The training history for the inverse model trained with 6,000 datasets further confirmed stable convergence (Fig. 9A). The training loss rapidly decreases during the first few hundred epochs and shows little change after approximately 1,000 epochs whereas the validation loss stabilizes around 2,000 epochs. Although the validation loss was slightly higher than the training loss, the difference between them remained small, suggesting that the inverse model was sufficiently generalizable for practical use.

The inverse model trained with 6,000 datasets showed good performance on the test datasets. The inlet flow velocity, U_0, and flow duration, T_{d}, were estimated with high accuracy, with normalized SMAPE values of 36.8% and 27.4%, respectively (Fig. 9D, F, Table 3). The suspended sediment concentrations, $C_{0,1}$ and $C_{0,2}$, were predicted with reasonable accuracy, with SMAPE values of 32.0% and 21.9%, respectively (Fig. 9B, C, Table 3).

In contrast, the flow thickness at inlet, h_0, was slightly more difficult to estimate than the other input parameters (Fig. 9E). The parameter h_0 had a slightly higher SMAPE values than the other parameters, 45.0% (Table 3).

Effects of Sampling Point Configuration and Observational Noise on Inversion Performance

As the sampling window was progressively extended from upstream to downstream, the inverse analysis performance saturated at approximately 50 sampling points (Fig. 10). The loss values gradually decreased as the number of sampling points increased from 10 to 50, with the validation loss decreasing from 0.031 at 10 sampling points to 0.020 at 50 sampling points. Extending the sampling window further downstream did not significantly improve inversion performance. Between 50 and 70 sampling points, the validation loss changed by a maximum of only 2.9×10^{-4}. Therefore, in the following evaluation of inversion performance with increasing numbers of sampling points in the transverse direction, the sampling range in the longitudinal direction was fixed to that corresponding to 50 sampling points, while the number of sampling points in the transverse direction was increased (Fig. 4).

The DNN-based inverse model trained with 6,000 datasets showed stable performance across a limited number of sampling points along the transverse direction (Fig. 11). The minimum training loss decreased across the range of sampling points, from approximately 0.0197 to 0.0116. In contrast, the minimum validation loss showed a smaller decrease than the training loss, declining from 0.0262 to 0.0225. This small variation of validation loss suggests that the inverse model retained broadly similar predictive skill even under sparse sampling and that additional sampling points provided only limited improvement in generalization.

Moreover, the performance of the inversion using the inverse model trained with 6,000 training datasets does not degrade significantly for noisy input data. As the value of r increases, SMAPE shows an increasing trend: it is 32.5% at $r = 0.01$ and 41.7% at $r = 0.2$, with a difference of 9.2% (Fig. 12). Although these values are larger than those reported by Fujishima and Naruse (2026), they exhibit a similar trend; namely, SMAPE increases monotonically as r increases. The DNN-based inverse model developed by Fujishima and Naruse (2026) shows that SMAPE increases from 27.9% to 30.1% within the range of r from 0.01 to 0.2 with a difference of 2.2% (Fig. 12). Although the inverse model in this study exhibits slightly higher SMAPE values than that of Fujishima and Naruse (2026), it shows similar performance change over the same range of r.

DISCUSSION

Behavior of Turbidity Currents and Turbidite Features in Confined Basins

The forward simulations reproduced features seen across different experiments and in natural settings. Reece et al. (2024, 2025) conducted three-dimensional flume experiments in a topography based on salt-withdrawal minibasins on the Gulf Coast, in which they generated turbidity currents. They showed that the inflowing turbidity currents were reflected from the distal slope, generating eddies. The numerical experiments in this study also produced eddies due to reflection by the downstream barrier (Fig. 5D, E, F).

Furthermore, distributary channels have been documented in Basin IV of the Brazos–Trinity intraslope system (Beaubouef et al. 2003b; Prather et al. 2012); similarly, our forward simulations also produced channels with unsteady pathways, resembling those formed within that minibasin (Fig. 6F).

These results suggest that the forward model captures some key aspects of flow dynamics and reproduces depositional features relevant to natural systems. The inversion framework trained with datasets generated by this forward model may therefore also be applicable to turbidites in natural confined basins, although further evaluation against flume experiments and natural systems is required.

Performance of the Inverse Model Applied to Turbidites in Confined Basins

The most significant outcome of the inversion experiments is that the DNN-based inverse model maintains robust predictive skill in confined basins despite limited training data, sparse sampling, and substantial observational noise. Although the forward simulations incorporate horizontally two-dimensional flow fields and complex topography, the number of training datasets required to achieve saturation in inversion accuracy is comparable to that of previous models.

Despite its higher dimensionality, the developed in this study required only a practical number of training datasets. The previous one-dimensional inverse model required more than 2,000 datasets to achieve sufficient performance (Cai and Naruse 2021; Naruse and Nakao 2021). Furthermore, the inverse model developed in this study achieved high predictive skill with a similarly practical number of training datasets. In addition, the inverse model for confined basins requires significantly fewer training datasets than the previous horizontally two-dimensional inverse model for unconfined basins, which used 10,000 training datasets (Fujishima and Naruse 2026).

Another major advantage of the proposed inversion framework is the computational efficiency, both in generating training datasets through parallel forward simulations and in rapidly estimating the input parameters of turbidity currents. Because the forward simulations can be performed independently, the computational cost remains tractable, enabling the generation of sufficiently large training datasets within realistic time frames. Other inversion methods for gravity flows, such as Markov Chain Monte Carlo methods (Moretti et al. 2020; Kameda and Okamoto 2021), surrogate management methods (Lesshafft et al. 2011), genetic algorithms (Nakao et al. 2020), and interior-point line-search filter method with adjoint method (Parkinson et al. 2017), require a large number of iterative forward simulations that cannot be easily parallelized. In contrast, the forward simulations used to generate the training datasets in the proposed framework can be fully parallelized. In this study, 14,500 training datasets were generated in less than one week using parallel forward simulations on five computers with a total 130 CPU cores, although the computational time depends on the grid spacing and Courant number. Therefore, our approach successfully enables the efficient development of an inverse model for turbidites in confined basins, similar to the DNN-based inverse model for unconfined basins (Fujishima and Naruse 2026). Once trained, the DNN-based inverse model can rapidly estimate the initial conditions of turbidity currents from observed deposit characteristics without requiring a case-by-case search through the forward-model results. This avoids the time-consuming process of manually exploring numerous possible combinations of input parameters. If we were to perform a case-by-case search with 10 variations for five parameters of the forward model, we would have to perform 10^5 calculations. In comparison, 6,000 is an overwhelmingly small number. In the future, if we increase the number of grain size classes in the model, the number of calculations required for a case-by-case search will increase exponentially, so the advantages of using a DNN will become more pronounced. This demonstrates the computational feasibility of applying the DNN-based inverse framework to naturally confined basins.

One of the important outcomes of this study is the robustness of the inversion framework to observational noise. Even when random noise with a standard deviation up to 20% of the input data was introduced, the mean SMAPE did not change significantly. This tolerance indicates that the model does not depend on highly precise measurements of bed thickness but instead extracts features of spatially distributed deposits. This robustness is particularly important when applying the inverse method to confined-basin deposits in the field, because measurement errors are inevitable in measurements of bed thickness and grain-size analyses.

Differences in inversion accuracy among the reconstructed input parameters of the forward model can be interpreted in terms of the sensitivity of the forward model. Flow duration T_d strongly influenced patterns of deposit thickness in confined basins, making it easier for the DNN to infer T_d from deposit features (Fig. 7A, E). Flow velocity, U_0, and suspended sediment concentrations, $C_{0,1}$ and $C_{0,2}$, had also large influences on the distribution of the deposit thickness (Fig. 7A, B, C); therefore, the inverse model reconstructed these parameters accurately. By contrast, the flow thickness h_0 produces more subtle depositional signatures, particularly on the basin plain (Fig. 7A, D). Therefore, the deposit features provide limited information for reconstructing h_0, resulting in a larger reconstruction error. These trends are consistent with those observed in unconfined-basin inversions (Fujishima and Naruse 2026), suggesting that the DNN captures physically meaningful relationships between flow dynamics to depositional architecture.

The results of this study indicate that the inverse model achieves higher performance when sampling points are located in areas where bed thickness varies substantially. In the present study, the inversion performance was saturated when the number of sampling points in the longitudinal direction reached 50 (Fig. 10). Forward calculations show that a channel is formed in this region (Fig. 6), resulting in more pronounced variations in bed thickness than in the other regions. Furthermore, inverse analyses were performed using sampling windows at different locations within the basin (Fig. C1), with the highest performance achieved when the sampling window was placed within the channel region in Figures 6 and 7 (Fig. C2; see Appendix C for details). In contrast, the downstream region, where the sampling point configuration had a relatively small influence on inversion performance, exhibited relatively little variation in bed thickness (Figs. 6, 7). A similar trend was reported by Fujishima and Naruse (2026). Their study evaluated the performance of an inverse model using flume experiments conducted in unconfined basins. The inverse model showed high performance for experimental turbidites characterized by greater spatial variation in thickness, whereas inversion was more difficult for turbidites with smaller thickness and limited spatial variation. These findings suggest that sampling should preferably be focused on areas characterized by greater variations in bed thickness when conducting inversion. This tendency is unlikely to be specific to DNN-based inverse models. Existing inverse models generally adopt the same fundamental framework of estimating hydraulic conditions from information contained in the deposits (Falcini et al. 2009; Lesshafft et al. 2011; Parkinson et al. 2017; Moretti et al. 2020; Kameda and Okamoto 2021). Therefore, the difficulty of inversion in regions with limited variation in bed thickness may represent a fundamental limitation of the inverse problem itself, rather than a characteristic specific to DNN-based inversion approaches.

Field Applicability and Significance of the Inversion Method Proposed in This Study

The inversion framework proposed in this study derives its predictive performance primarily from global patterns in deposit geometry rather than from fine-scale morphological details. This characteristic enables the model to remain effective even under complex and unsteady channel conditions typical of confined basins. Such complex channel morphologies are commonly observed in natural systems, for example in Basin IV of the Brazos–Trinity intraslope system (Beaubouef et al. 2003b). The ability of the inversion framework to rely on integrated depositional signals, rather than detailed channel geometry, likely explains its stable performance under these conditions.

Although natural confined basins exhibit substantial variability in geometry and formation processes, the inversion framework developed in this study can be adapted to basin-specific conditions. Basin geometry is a primary control on turbidity-current behavior, and therefore must be explicitly incorporated into inverse analysis. Natural basins display a wide range of morphologies, for example those associated with salt tectonics in the Gulf Coast, where complex minibasins and salt domes generate large variations in basin shape and depth (Kramer and Shedd 2017; Reece and Straub 2025; Reece et al. 2025). In this respect, the proposed framework is highly flexible, as it allows basin topography to be freely prescribed for individual settings.

In addition to geometry, sediment-transport pathways and source locations also vary among basins and may be poorly constrained. For example, the Hydrate Ridge west basin on the Cascadia margin lacks distinct feeder channels (Goldfinger et al. 2013). The present framework can accommodate such uncertainty because the inlet location can be treated as an output parameter, enabling inverse analysis even when sediment sources are not well defined.

However, more accurate forward models are required in settings where vertical velocity and momentum play an important role. The forward model adopted in this study is a depth-averaged model and therefore does not account for variations in physical quantities in the vertical direction (e.g., Parker et al. 1986; Meiburg and Kneller 2010). Consequently, the DNN-inverse model trained using a depth-averaged model cannot capture the vertical flow structures.

Previous experimental studies have demonstrated vertical variations in turbidity currents within confined basins, including depth-dependent flow directions and velocity profiles in slot-like confined minibasins due to reflection, pushing of the interface between the outbound flow and the return flow by an internal wave, and collapse of part of the flow from the slope (Sequeiros et al. 2009; Patacci et al. 2015), and upwelling jets in bowl-shaped minibasins caused by conversion of turbidity currents toward the center of circulation cell (Reece et al. 2024). Such vertical variations can also occur in natural settings, where fault-related topographies (e.g., Alves et al. 2009; Baudouy et al. 2021) and salt-tectonic mounds form barriers within confined basins (Ge et al. 2020). In such settings where barriers exist in the basin, the vertical effects described above are expected to occur locally within the basins. Moreover, it has been reported that the basal dense layer, which is caused by vertical density stratification (e.g., Sher and Woods 2015; Paull et al. 2018; Ma et al. 2026), can be trapped by such topographic barriers within the basin (e.g., Englert et al. 2024). Such phenomena related to vertically structured flow fields cannot be reproduced by depth-averaged models. To account for these effects, high-fidelity three-dimensional models, such as direct numerical simulation (DNS) and large-eddy simulation (LES), are required.

However, the DNN-based inversion framework can be applied to such settings by changing the forward model to a high-fidelity model because it does not depend on a specific model. As pointed out in previous studies, when a different forward model is adopted, the DNN-based inversion model can simply be retrained using training datasets generated by that forward model (Naruse and Nakao 2021; Fujishima and Naruse 2026). This flexibility allows the framework to employ different forward models depending on the specific objectives and to readily incorporate improved forward models.

Despite the limitations discussed above, the depth-averaged model remains widely accepted. The depth-averaged model has relatively low computational costs while providing sufficient predictive performance. Especially at the field scale, depth-averaged models are widely used because they are computationally less demanding than high-fidelity models while providing results that are consistent with experimental deposits and field observations (e.g., Imran et al. 1998; Bradford and Katopodes 1999; Fildani et al. 2006; Lai et al. 2015). Thus, from a practical perspective, the depth-averaged model would currently be the first choice as the forward model. However, with future advances in computational power and the development of more efficient numerical methods, inversion using high-fidelity models may also become feasible.

The proposed inversion method is resilient to sparse spatial sampling of deposits, which is an important practical consideration for outcrop- and core-based studies. In this study, as few as 30 sampling points were sufficient to perform the inversion. Therefore, the inversion approach may be applicable to field-scale turbidites. For example, Tokuhashi (1979) documented turbidites at 26 locations over a distance of 30 km in the Kiyosumi Formation on the Boso Peninsula, Japan, and correlated them using tuffaceous key beds. Such datasets satisfy the sampling requirements of the present framework, suggesting that inverse analysis may be feasible for well-exposed field successions. In marine core studies, the number of sampling points per basin is typically more limited. However, it is possible to interpolate core data using seismic data (e.g., Kioka et al. 2019). These considerations suggest that the proposed inversion framework can be realistically applied to both outcrop and marine core datasets.

The inversion framework developed in this study provides a means to quantitatively link turbidity-current dynamics to the resulting depositional architecture in confined basins. Depositional features in such settings are highly variable. For example, distributary channel systems are observed in minibasins in the Gulf Coast (Beaubouef et al. 2003b), whereas relatively simple, laterally thinning turbidites occur in other settings such as the Sorbas basin (Haughton 1994) and the Nankai Trough prism slope (Ashi et al. 2014). Although these differences are widely recognized, the flow conditions responsible for these contrasting morphologies remain poorly constrained. By enabling the reconstruction of flow parameters from deposits, the proposed inversion framework offers a quantitative approach to identifying the physical controls on this depositional diversity. This capability is critical because it provides a means to quantitatively constrain the hydraulic conditions of the turbidity currents that generated the observed deposits.

Building on this capability, the inversion framework developed in this study holds strong potential for advancing quantitative marine paleoseismology by constraining the magnitude of sediment transport associated with earthquakes and tsunamis. Following the 2011 Tohoku-Oki earthquake and tsunami, turbidites were observed over a wide area of the trench slope (e.g., Arai et al. 2013; Kanamatsu et al. 2017; Ikehara et al. 2020), and within the Japan Trench (e.g., McHugh et al. 2016; Kioka et al. 2019; Strasser et al. 2024). These observations raise the possibility that magnitudes of earthquakes are reflected in the hydraulic conditions of the resulting turbidity currents.

This hypothesis can be tested by applying the inverse model developed in this study to turbidites associated with earthquakes of known magnitude and evaluating the relationship between the reconstructed flow conditions and earthquake magnitude. This approach is feasible because inverse modeling can reconstruct these conditions from turbidites, as demonstrated here and in previous research (e.g., Cai and Naruse 2021; Fujishima and Naruse 2026). If robust relationships can be established, the inverse model could provide a quantitative basis for investigating past earthquake histories from earthquake-induced turbidites preserved on the deep-sea floor.

Furthermore, this approach can be extended by integrating the inverse analysis of turbidity currents with forward models of seismic ruptures and tsunami generation. For tsunami-induced turbidity currents, for example, tsunami propagation can be calculated from source fault parameters (e.g., Goto et al. 2012; Baba et al. 2015), and the resulting suspended sediment concentration can subsequently be used to define the initial conditions for forward calculation of the turbidity current. By generating training datasets using such an integrated forward model, it may be possible to establish a quantitative relationship between source fault parameters and tsunami-induced turbidites. This coupled approach could therefore provide a framework for quantitatively linking fault parameters to tsunami and turbidity-current dynamics and, ultimately, to the resulting turbidite characteristics.

CONCLUSIONS

This study developed a horizontally two-dimensional DNN inversion framework capable of reconstructing flow conditions of turbidity currents in confined basins. Forward simulations reproduced key characteristics of confined-basin turbidity currents, including ponding and channelization.

The DNN-based inverse model demonstrated high inversion performance using a small number of training datasets. The performance of inverse model saturated at only 5,000 training datasets and successfully reconstructed the inlet conditions with reasonable accuracy. Input parameters that strongly influenced the depositional features, such as flow velocity, suspended sediment concentration and flow duration, were estimated with high precision, whereas parameters with weaker depositional signatures, such as flow thickness, exhibited slightly larger errors.

The inversion framework exhibited notable robustness to sparse spatial sampling and observational noise, reflecting its reliance on integrated, basin-scale depositional patterns rather than fine-scale channel morphology. The inverse model required only a small number of sampling points to achieve performance saturation and showed only a 9.2% change in SMAPE under noise with a standard deviation of 0.2. This robustness suggests that the model is well-suited for applications in natural confined basins.

By enabling quantitative reconstruction of flow conditions from turbidites, the proposed framework provides a basis for linking depositional records to the processes that generate them. When integrated with models of tsunami generation, seismic shaking, and sediment transport, this approach offers a pathway toward reconstructing fault slip and earthquake magnitude from sedimentary records. Future work should focus on validating the inversion framework using experimental and natural datasets, particularly through comparison with controlled flume experiments and well-constrained field cases.

DATA AVAILABILITY STATEMENT

The training and test datasets, trained models, inversion results, and scripts to draw the figures are available on Zenodo at https://doi.org/10.5281/zenodo.19703915. The result of sensitivity test and example forward simulation were stored at https://doi.org/10.5281/zenodo.20109645. The open-source software *turb2d* (v.1.0.1) used in this study to implement the forward model is archived at https://doi.org/10.5281/zenodo.20116549 and its GitHub repository is available at https://github.com/fujishimaseiya/turb2d. The source code for the development and verification of DNN-based inverse model for turbidity currents, *nninv1d* (v1.0.1), is archived at https://doi.org/10.5281/zenodo.20116662 and its GitHub repository is hosted at https://github.com/fujishimaseiya/nninv1d.

CONFLICTS OF INTEREST

The authors declare no conflicts of interest.

ACKNOWLEDGEMENTS

The authors would like to thank Prof. Christopher Stevenson and the anonymous reviewer for their constructive comments and suggestions, which helped improve the manuscript. This work was supported by JST, the establishment of university fellowships towards the creation of science technology innovation (Grant Number JPMJFS2123), JST SPRING (Grant Number JPMJSP2110). Additional supports were provided by the Sediment Dynamics Research Consortium, sponsored by INPEX, JAPEX and JOGMEC.

AI STATEMENT

The authors used ChatGPT (GPT-5.6 Luna) and Grammarly for English language editing, including grammar correction, sentence restructuring, and improvement of readability.

NOTATION

b Bias

$C_{0,1}$ Suspended sediment concentration at the inlet for 20 μm particles

$C_{0,2}$ Suspended sediment concentration at the inlet for 3 μm particles

$D_{\mathrm{s},1}$ Partcile diameter (50 μm)

$D_{\mathrm{s},2}$ Partcile diameter (3 μm)

h_0 Flow thickness at the inlet

M Number of input parameters of the forward model

m Index of an input parameter

N Number of test datasets

n Index of a test dataset

r Noise ratio

T_{d} Flow duration

U_0 Flow velocity at the inlet

x_{test} Test data without noise

$x_{\mathrm{test,noise}}$ Test data with noise

y_n True value in the nth test data

$y_{\mathrm{p}n}$ Predicted value of nth test data

y_{mn} True value of the mth parameter in the nth test dataset

$y_{\mathrm{p}mn}$ Predicted value of the mth parameter in the nth test dataset

Δx Grid spacing

ϵ Random value sampled from a standard normal distribution

REFERENCES

Alves, T.M., Cartwright, J., and Davies, R.J., 2009, Faulting of salt-withdrawal basins during early halokinesis: Effects on the Paleogene Rio Doce Canyon system (Espírito Santo Basin, Brazil): AAPG Bulletin, v. 93, p. 617–652, doi:10.1306/02030908105.

Arai, K., Inoue, T., Ikehara, K., and Sasaki, T., 2014, Episodic subsidence and active deformation of the forearc slope along the Japan Trench near the epicenter of the 2011 Tohoku Earthquake: Earth and Planetary Science Letters, v. 408, p. 9–15, doi:10.1016/j.epsl.2014.09.048.

Arai, K., Naruse, H., Miura, R., Kawamura, K., Hino, R., Ito, Y., Inazu, D., Yokokawa, M., Izumi, N., Murayama, M., and Kasaya, T., 2013, Tsunami-generated turbidity current of the 2011 Tohoku-Oki earthquake: Geology, v. 41, p. 1195–1198, doi:10.1130/G34777.1.

Ashi, J., Sawada, R., Omura, A., and Ikehara, K., 2014, Accumulation of an earthquake-induced extremely turbid layer in a terminal basin of the Nankai accretionary prism: Earth, Planets and Space, v. 66, p. 51, doi:10.1186/1880-5981-66-51.

Baba, T., Takahashi, N., Kaneda, Y., Ando, K., Matsuoka, D., and Kato, T., 2015, Parallel Implementation of Dispersive Tsunami Wave Modeling with a Nesting Algorithm for the 2011 Tohoku Tsunami: Pure and Applied Geophysics, v. 172, p. 3455–3472, doi:10.1007/s00024-015-1049-2.

Baudouy, L., Haughton, P.D.W., and Walsh, J.J., 2021, Evolution of a Fault-Controlled, Deep-Water Sub-Basin, Tabernas, SE Spain: Frontiers in Earth Science, v. Volume 9-2021, https://www.frontiersin.org/journals/earth-science/articles/10.3389/feart.2021.767286.

Beaubouef, R.T., Abreu, V., and Adair, N.L., 2003a, Ultra-High Resolution 3-D Characterization of Deep-Water Deposits-I: A New Approach to Understanding the Stratigraphic Evolution of Intra-Slope Depositional Systems: AAPG Annual Meeting, Search and Discovery Article, p. 40084.

Beaubouef, R.T., Wagoner, J.C.V., and Adair, N.L., 2003b, Ultra-High Resolution 3-D Characterization of Deep-Water Deposits-II: Insights into the Evolution of a Submarine Fan and Comparisons with River Deltas: AAPG Annual Meeting, Search and Discovery Article, p. 40085.

Bowen, A.J., Normark, W.R., and Piper, D.J.W., 1984, Modelling of turbidity currents on Navy Submarine Fan, California Continental Borderland: Sedimentology, v. 31, p. 169–185, doi:10.1111/j.1365-3091.1984.tb01957.x.

Bradford, S.F., and Katopodes, N.D., 1999, Hydrodynamics of Turbid Underflows. I: Formulation and Numerical Analysis: Journal of Hydraulic Engineering, v. 125, p. 1006–1015, doi:10.1061/(ASCE)0733-9429(1999)125:10(1006).

Cai, Z., and Naruse, H., 2021, Inverse Analysis of Experimental Scale Turbidity Currents Using Deep Learning Neural Networks: Journal of Geophysical Research: Earth Surface, v. 126, p. e2021JF006276, doi:10.1029/2021JF006276.

Englert, R.G., Hubbard, S.M., Romans, B.W., Kaempfe, S., Bell, D., Nesbit, P.R., and Stright, L., 2024, Flow dynamics as Froude-supercritical turbidity currents encounter metre-scale slope minibasin topography: The Depositional Record, v. 10, p. 527–558, doi:10.1002/dep2.262.

Falcini, F., Marini, M., Milli, S., and Moscatelli, M., 2009, An inverse problem to infer paleoflow conditions from turbidites: Journal of Geophysical Research: Oceans, v. 114, p. 2009JC005294, doi:10.1029/2009JC005294.

Felletti, F., 2002, Complex bedding geometries and facies associations of the turbiditic fill of a confined basin in a transpressive setting (Castagnola Fm., Tertiary Piedmont Basin, NW Italy): Sedimentology, v. 49, p. 645–667, doi:10.1046/j.1365-3091.2002.00467.x.

Fildani, A., Normark, W.R., Kostic, S., and Parker, G., 2006, Channel formation by flow stripping: large-scale scour features along the Monterey East Channel and their relation to sediment waves: Sedimentology, v. 53, p. 1265–1287, doi:10.1111/j.1365-3091.2006.00812.x.

Fujishima, S., and Naruse, H., 2026, Experimental Verification of a Two-Dimensional Inverse Method for Turbidity Currents Using a Deep Neural Network: Journal of Geophysical Research: Machine Learning and Computation, v. 3, p. e2025JH000952, doi:10.1029/2025JH000952.

Ge, Z., Gawthorpe, R.L., Rotevatn, A., Zijerveld, L., A.-L. Jackson, C., and Oluboyo, A., 2020, Minibasin depocentre migration during diachronous salt welding, offshore Angola: Basin Research, v. 32, p. 875–893, doi:10.1111/bre.12404.

Goldfinger, C., 2011, Submarine Paleoseismology Based on Turbidite Records: Annual Review of Marine Science, v. 3, p. 35–66, doi:10.1146/annurev-marine-120709-142852.

Goldfinger, C., Galer, S., Beeson, J., Hamilton, T., Black, B., Romsos, C., Patton, J., Nelson, C.H., Hausmann, R., and Morey, A., 2017, The importance of site selection, sediment supply, and hydrodynamics: A case study of submarine paleoseismology on the northern Cascadia margin, Washington USA: Marine Geology, v. 384, p. 4–46, doi:10.1016/j.margeo.2016.06.008.

Goldfinger, C., Morey, A.E., Black, B., Beeson, J., Nelson, C.H., and Patton, J., 2013, Spatially limited mud turbidites on the Cascadia margin: segmented earthquake ruptures? Natural Hazards and Earth System Sciences, v. 13, p. 2109–2146, doi:10.5194/nhess-13-2109-2013.

Goto, K., Fujima, K., Sugawara, D., Fujino, S., Imai, K., Tsudaka, R., Abe, T., and Haraguchi, T., 2012, Field measurements and numerical modeling for the run-up heights and inundation distances of the 2011 Tohoku-oki tsunami at Sendai Plain, Japan:

Earth, Planets and Space, v. 64, p. 1247–1257, doi:10.5047/eps.2012.02.007.

Haughton, P.D.W., 1994, Deposits of Deflected and Ponded Turbidity Currents, Sorbas Basin, Southeast Spain: Journal of Sedimentary Research, v. A64, p. 233–246, doi:10.1306/D4267D6B-2B26-11D7-8648000102C1865D.

Hiscott, R.N., 1994, Loss of capacity, not competence, as the fundamental process governing deposition from turbidity currents: Journal of Sedimentary Research, v. A64, p. 209–214, doi:10.2110/jsr.64.209.

Hudec, M.R., and Jackson, M.P.A., 2007, Terra infirma: Understanding salt tectonics: Earth-Science Reviews, v. 82, p. 1–28, doi:10.1016/j.earscirev.2007.01.001.

Hudec, M.R., Jackson, M.P.A., and Schultz-Ela, D.D., 2009, The paradox of minibasin subsidence into salt: Clues to the evolution of crustal basins: GSA Bulletin, v. 121, p. 201–221, doi:10.1130/B26275.1.

Ikehara, K., Usami, K., Irino, T., Omura, A., Jenkins, R.G., and Ashi, J., 2021, Characteristics and distribution of the event deposits induced by the 2011 Tohoku-oki earthquake and tsunami offshore of Sanriku and Sendai, Japan: Sedimentary Geology, v. 411, p. 105791, doi:10.1016/j.sedgeo.2020.105791.

Ikehara, K., Usami, K., and Kanamatsu, T., 2020, Repeated occurrence of surface-sediment remobilization along the landward slope of the Japan Trench by great earthquakes: Earth, Planets and Space, v. 72, p. 114, doi:10.1186/s40623-020-01241-y.

Imran, J., Parker, G., and Katopodes, N., 1998, A numerical model of channel inception on submarine fans: Journal of Geophysical Research: Oceans, v. 103, p. 1219–1238, doi:10.1029/97JC01721.

Jackson, C.A.-L., Duffy, O.B., Fernandez, N., Dooley, T.P., Hudec, M.R., Jackson, M.P.A., and Burg, G., 2020, The stratigraphic record of minibasin subsidence, Precaspian Basin, Kazakhstan: Basin Research, v. 32, p. 739–763, doi:10.1111/bre.12393.

Kameda, J., and Okamoto, A., 2021, 1-D inversion analysis of a shallow landslide triggered by the 2018 Eastern Iburi earthquake in Hokkaido, Japan: Earth, Planets and Space, v. 73, p. 116, doi:10.1186/s40623-021-01443-y.

Kanamatsu, T., Usami, K., McHugh, C.M.G., and Ikehara, K., 2017, High-resolution chronology of sediment below CCD based on Holocene paleomagnetic secular variations in the Tohoku-oki earthquake rupture zone: Geochemistry, Geophysics, Geosystems, v. 18, p. 2990–3002, doi:10.1002/2017GC006878.

Kane, I.A., McGee, D.T., and Jobe, Z.R., 2012, Halokinetic effects on submarine channel equilibrium profiles and implications for facies architecture: conceptual model illustrated with a case study from Magnolia Field, Gulf of Mexico: Geological Society, London, Special Publications, v. 363, p. 289–302, doi:10.1144/SP363.13.

Khan, S.M., and Imran, J., 2008, Numerical Investigation of Turbidity Currents Flowing Through Minibasins on the Continental Slope: Journal of Sedimentary Research, v. 78, p. 245–257, doi:10.2110/jsr.2008.031.

Kioka, A., Schwestermann, T., Moernaut, J., Ikehara, K., Kanamatsu, T., Eglinton, T.I., and Strasser, M., 2019, Event Stratigraphy in a Hadal Oceanic Trench: The Japan Trench as Sedimentary Archive Recording Recurrent Giant Subduction Zone Earthquakes and Their Role in Organic Carbon Export to the Deep Sea: Frontiers in Earth Science, v. 7, p. 319, doi:10.3389/feart.2019.00319.

Komar, P.D., 1985, The hydraulic interpretation of turbidites from their grain sizes and sedimentary structures: Sedimentology, v. 32, p. 395–407, doi:10.1111/j.1365-3091.1985.tb00519.x.

Kramer, K.V., and Shedd, W.W., 2017, A 1.4-Billion-Pixel Map of the Gulf of

Mexico Seafloor: Eos, v. 98, doi:10.1029/2017EO073557.

Lai, Y.G., Huang, J., and Wu, K., 2015, Reservoir Turbidity Current Modeling with a Two-Dimensional Layer-Averaged Model: Journal of Hydraulic Engineering, v. 141, doi:10.1061/(asce)hy.1943-7900.0001041.

Lamb, M.P., Hickson, T., Marr, J.G., Sheets, B., Paola, C., and Parker, G., 2004, Surging Versus Continuous Turbidity Currents: Flow Dynamics and Deposits in an Experimental Intraslope Minibasin: Journal of Sedimentary Research, v. 74, p. 148–155, doi:10.1306/062103740148.

Lesshafft, L., Meiburg, E., Kneller, B., and Marsden, A., 2011, Towards inverse modeling of turbidity currents: The inverse lock-exchange problem: Computers & Geosciences, v. 37, p. 521–529, doi:10.1016/j.cageo.2010.09.015.

Ma, H., Deng, G., Chen, X., Wang, Y., McElroy, B., Nittrouer, J., Zhang, Y., Iwasaki, T., Cartigny, M., and Fu, X., 2026, In situ evidence of self-accelerating turbidity currents: Proceedings of the National Academy of Sciences, v. 123, p. e2601534123, doi:10.1073/pnas.2601534123.

McHugh, C.M., Kanamatsu, T., Seeber, L., Bopp, R., Cormier, M.-H., and Usami, K., 2016, Remobilization of surficial slope sediment triggered by the A.D. 2011 Mw 9 Tohoku-Oki earthquake and tsunami along the Japan Trench: Geology, v. 44, p. 391–394, doi:10.1130/G37650.1.

Meiburg, E., and Kneller, B., 2010, Turbidity Currents and Their Deposits: Annual Review of Fluid Mechanics, v. 42, p. 135–156, doi:10.1146/annurev-fluid-121108-145618.

Moretti, L., Mangeney, A., Walter, F., Capdeville, Y., Bodin, T., Stutzmann, E., and Le Friant, A., 2020, Constraining landslide characteristics with Bayesian inversion of field and seismic data: Geophysical Journal International, v. 221, p. 1341–1348, doi:10.1093/gji/ggaa056.

Nakao, K., Naruse, H., and Tokuhashi, S., 2020, Inverse analysis to reconstruct hydraulic conditions of non-steady turbidity currents: Application to an ancient turbidite of the Kiyosumi Formation of the Awa Group, Boso Peninsula, central Japan: EarthArXiv, doi:10.31223/X51S3S.

Naruse, H., and Nakao, K., 2021, Inverse modeling of turbidity currents using an artificial neural network approach: verification for field application: Earth Surface Dynamics, v. 9, p. 1091–1109, doi:10.5194/esurf-9-1091-2021.

Parker, G., Fukushima, Y., and Pantin, H.M., 1986, Self-accelerating turbidity currents: Journal of Fluid Mechanics, v. 171, p. 145–181, doi:10.1017/S0022112086001404.

Parkinson, S.D., Funke, S.W., Hill, J., Piggott, M.D., and Allison, P.A., 2017, Application of the adjoint approach to optimise the initial conditions of a turbidity current with the AdjointTurbidity 1.0 model: Geoscientific Model Development, v. 10, p. 1051–1068, doi:10.5194/gmd-10-1051-2017.

Patacci, M., Haughton, P.D.W., and Mccaffrey, W.D., 2015, Flow Behavior of Ponded Turbidity Currents: Journal of Sedimentary Research, v. 85, p. 885–902, doi:10.2110/jsr.2015.59.

Paull, C.K., Talling, P.J., Maier, K.L., Parsons, D., Xu, J., Caress, D.W., Gwiazda, R., Lundsten, E.M., Anderson, K., Barry, J.P., Chaffey, M., O'Reilly, T., Rosenberger, K.J., Gales, J.A., Kieft, B., McGann, M., Simmons, S.M., McCann, M., Sumner, E.J., Clare, M.A., and Cartigny, M.J., 2018, Powerful turbidity currents driven by dense basal layers: Nature Communications, v. 9, p. 4114, doi:10.1038/s41467-018-06254-6.

Pizer, C., Ikehara, K., Keep, M., Kioka, A., Kodaira, S., Miura, R., Moernaut, J., Nakamura, Y., and Strasser, M., 2025, Geological evidence for repeated slip-to-the-trench style megathrust earthquakes at the Japan Trench: Geology, v. 53, p. 370–374, doi:10.1130/G52797.1.

Posamentier, H.W., 2003, Depositional elements associated with a basin floor channel-levee system: case study from the Gulf of Mexico: Marine and Petroleum Geology, v. 20, p. 677–690, doi:10.1016/j.marpetgeo.2003.01.002.

Posamentier, H.W., and Walker, R.G., 2006, Deep-Water Turbidites and Submarine Fans, *in* Posamentier, H.W. and Walker, R.G. eds., Facies Models Revisited: SEPM, SEPM Special Publication 84, p. 397–520, doi:10.2110/pec.06.84.0399.

Prather, B.E., 2000, Calibration and visualization of depositional process models for above-grade slopes: a case study from the Gulf of Mexico: Marine and Petroleum Geology, v. 17, p. 619–638, doi:10.1016/S0264-8172(00)00015-5.

Prather, B.E., Pirmez, C., and Winker, C.D., 2012, Stratigraphy of Linked Intraslope Basins: Brazos–Trinity System Western Gulf of Mexico, *in* Prather, B.E., Deptuck, M.E., Mohrig, D., Hoorn, B.V., and Wynn, R.B. eds., Application of the Principles of Seismic Geomorphology to Continental Slope and Base-of-Slope Systems: Case Studies from SeaFloor and Near-Sea Floor Analogues: SEPM, SEPM Special Publication 99, p. 83–109, doi:10.2110/pec.12.99.0083.

Reece, J.K., Dorrell, R.M., and Straub, K.M., 2024, Circulation of hydraulically ponded turbidity currents and the filling of continental slope minibasins: Nature Communications, v. 15, p. 2075, doi:10.1038/s41467-024-46120-2.

Reece, J.K., Dorrell, R.M., and Straub, K.M., 2025, Influence of flow discharge and minibasin shape on the flow behavior and depositional mechanics of ponded turbidity currents: Geological Society of America Bulletin, v. 137, p. 1797–1814, doi:10.1130/B37517.1.

Reece, J.K., and Straub, K.M., 2025, Statistics of Depressions Covering the Northern Gulf of Mexico Salt-Minibasin Province: Drivers and Strength of Bathymetric Self-Organization: Journal of Geophysical Research: Oceans, v. 130, p. e2024JC021726, doi:10.1029/2024JC021726.

Sequeiros, O.E., Spinewine, B., Garcia, M.H., Beaubouef, R.T., Sun, T., and Parker, G., 2009, Experiments on Wedge-Shaped Deep Sea Sedimentary Deposits in Minibasins and/or on Channel Levees Emplaced by Turbidity Currents. Part I. Documentation of the Flow: Journal of Sedimentary Research, v. 79, p. 593–607, doi:10.2110/jsr.2009.064.

Sher, D., and Woods, A.W., 2015, Gravity currents: entrainment, stratification and self-similarity: Journal of Fluid Mechanics, v. 784, p. 130–162, doi:10.1017/jfm.2015.576.

Spinewine, B., Sequeiros, O.E., Garcia, M.H., Beaubouef, R.T., Sun, T., Savoye, B., and Parker, G., 2009, Experiments on Wedge-Shaped Deep Sea Sedimentary Deposits in Minibasins and/or on Channel Levees Emplaced by Turbidity Currents. Part II. Morphodynamic Evolution of the Wedge and of the Associated Bedforms: Journal of Sedimentary Research, v. 79, p. 608–628, doi:10.2110/jsr.2009.065.

Strasser, M., Ikehara, K., Everest, J., Maeda, L., Hochmuth, K., Grant, H., Stewart, M., Okutsu, N., Sakurai, N., Yokoyama, T., Bao, R., Bellanova, P., Brunet, M., Cai, Z., Cattaneo, A., Hsiung, K.-H., Huang, J.-J., Ishizawa, T., Itaki, T., Jitsuno, K., Johnson, J.E., Kanamatsu, T., Keep, M., Kioka, A., Kölling, M., Luo, M., März, C., McHugh, C., Micallef, A., Nagahashi, Y., Pandey, D.K., Proust, J.-N., Rasbury, E.T., Riedinger, N., Satoguchi, Y., Sawyer, D.E., Seibert, C., Silver, M., Straub, S.M., Virtasalo, J., Wang, Y., Wu, T.-W., and Zellers, S.D., 2023, Expedition 386 summary: Japan Trench Paleoseismology, doi:10.14379/iodp.proc.386.2023.

Strasser, M., Ikehara, K., Pizer, C., Itaki, T., Satoguchi, Y., Kioka, A., McHugh, C., Proust, J.-N., Sawyer, D., IODP Expedition Management Team, and IODP Expedition 386 Expedition Science Party, 2024, Japan Trench event stratigraphy: First results from IODP giant piston coring in a deep-sea trench to advance subduction zone paleoseismology: Marine Geology, v. 477, p. 107387, doi:10.1016/j.margeo.2024.107387.

Tokuhashi, S., 1979, Three Dimensional Analysis of a Large Sandy-Flysch Body, Mio-Pliocene Kiyosumi Formation, Boso Peninsula, Japan: Memoirs of the Faculty of Science, Kyoto University. Series of geology and mineralogy, v. 46, p. 1–60.

Toniolo, H., Lamb, M., and Parker, G., 2006a, Depositional Turbidity Currents in Diapiric Minibasins on the Continental Slope: Formulation and Theory: Journal of Sedimentary Research, v. 76, p. 783–797, doi:10.2110/jsr.2006.071.

Toniolo, H., Parker, G., Voller, V., and Beaubouef, R.T., 2006b, Depositional Turbidity Currents in Diapiric Minibasins on the Continental Slope: Experiments—Numerical Simulation and Upscaling: Journal of Sedimentary Research, v. 76, p. 798–818, doi:10.2110/jsr.2006.072.

Violet, J., Sheets, B., Pratson, L., Paola, C., Beaubouef, R., and Parker, G., 2005, Experiment on Turbidity Currents and Their Deposits in a Model 3D Subsiding Minibasin: Journal of Sedimentary Research, v. 75, p. 820–843, doi:10.2110/jsr.2005.065.

Wang, X., Luthi, S.M., Hodgson, D.M., Sokoutis, D., Willingshofer, E., and Groenenberg, R.M., 2017, Turbidite stacking patterns in salt-controlled minibasins: Insights from integrated analogue models and numerical fluid flow simulations:

Sedimentology, v. 64, p. 530–552, doi:10.1111/sed.12313.

Winker, C.D., 1996, High-Resolution Seismic Stratigraphy of a Late Pleistocene Submarine Fan Ponded by Salt-Withdrawal Mini-Basins on the Gulf of Mexico Continental Slope: Offshore Technology Conference, Proceedings Papers, p. OTC-8024-MS, doi:10.4043/8024-MS.

FIG. 1.--- Framework for training and testing the inverse model (modified after Fujishima and Naruse 2026). First, training datasets were generated using the forward model. The inverse model was then trained using these datasets to learn the relationship between the sediment volume per unit area at sampling points and the input parameters of the forward model. The performance of the trained inverse model was evaluated using the test datasets.

FIG. 2.--- Initial topography for forward simulations of turbidity currents.

FIG. 3.--- Sampling points used to evaluate inverse model performance under different sampling point densities in the longitudinal direction. A) 10 points. B) 20 points. C) 30 points. D) 40 points. E) 50 points. F) 60 points. G) 70 points.

FIG. 4.--- Sampling points used to evaluate inverse model performance under different sampling point densities in the transverse direction. A) 10 points. B) 20 points. C) 30 points. D) 40 points. E) 50 points.

FIG. 5.--- Spatial and temporal variations in flow thickness in the example calculation at A) 20,000 seconds, B) 25,000 seconds, C) 50,000 seconds, D) 100,000 seconds, E) 200,000 seconds, and F) 300,000 seconds after the start of the calculation.

FIG. 6.--- Spatial and temporal variations in densimetric Froude number and bed thickness in the example calculation. A) Densimetric Froude number and B) Bed

thickness at 100,000 seconds. C) Densimetric Froude number and D) bed thickness at 200,000 seconds. E) Densimetric Froude number and F) bed thickness at 300,000 seconds.

FIG. 7.--- Effect of forward-model input parameters on simulated bed thickness. Each panel shows the distribution of bed thickness at the end of the simulation. A) Case 1 (base case). B) Case 2 (twice the suspended sediment concentration). C) Case 3 (twice the flow velocity). D) Case 4 (twice the flow thickness). E) Case 5 (twice the flow duration).

FIG. 8.--- Variation in inverse model performance with the number of training data.

FIG. 9.--- Training and test results of the inverse model trained on 6,000 datasets. A) Training history on 6,000 training datasets. B–F) show the estimation accuracy of the input parameters for the test datasets: B) Suspended sediment concentration (20 μm) at the inlet; C) Suspended sediment concentration (3 μm) at the inlet; D) Flow velocity at the inlet; E) Flow thickness at the inlet; F) Flow duration. The diagonal orange lines in B–F) indicate where the original values equal the reconstructed values. Points lying on these lines represent estimates with zero error.

FIG. 10.--- Effect of the number of sampling points along the longitudinal direction on inverse model performance.

FIG. 11.--- Effect of the number of sampling points along the transverse direction on inverse model performance.

FIG. 12.--- Comparison of inversion performance for noisy input data between the proposed model and the model of Fujishima and Naruse (2026). For each noise ratio r, ten noisy test datasets were generated and the inverse model was applied to estimate the forward-model input parameters, and the mean SMAPE was calculated from ten trials.

Appendix

Deep Neural Network-Based Inversion of Turbidites in Confined Basins

Seiya Fujihsima[1*] and Hajime Naruse[1]

[1] Department of Geology and Mineralogy, Division of Earth and Planetary Sciences, Graduate School of Science, Kyoto University, Kyoto, Japan

*Corresponding author (E-mail address: fujishima.seiya.z47@kyoto-u.jp)

APPENDIX A: FORWARD MODEL

Numerical Model of Turbidity Currents Based on Shallow-Water Equations

We employed a horizontally two-dimensional forward model based on the four-equation model (Parker et al. 1986). This model is based on the shallow-water equations, which consider layer-averaged flow parameters. The governing equations for turbidity currents consist of fluid mass conservation, suspended sediment mass conservation, fluid momentum conservation, and turbulent kinetic energy conservation, and are expressed as follows:

$$\frac{\partial h}{\partial t}+\frac{\partial Uh}{\partial x}+\frac{\partial Vh}{\partial y}=e_{\mathrm{w}}\sqrt{U^2+V^2}-d_w \tag{A1}$$

$$\frac{\partial C_i h}{\partial t}+\frac{\partial UC_i h}{\partial x}+\frac{\partial VC_i h}{\partial y}=w_{si}(F_i e_{si}-r_0 C_i) \tag{A2}$$

$$\frac{\partial Uh}{\partial t}+\frac{\partial U^2 h}{\partial x}+\frac{\partial UVh}{\partial y}=-\frac{1}{2}Rg\frac{\partial C_i h^2}{\partial \mathrm{x}}+RgC_{\mathrm{T}}\frac{\partial \eta_{\mathrm{T}}}{\partial x}$$
$$-c_{\mathrm{f}}U\sqrt{U^2+V^2}+\nu_{\mathrm{t}}\left(\frac{\partial^2 Uh}{\partial x^2}+\frac{\partial^2 Vh}{\partial y^2}\right) \tag{A3}$$

$$\frac{\partial Vh}{\partial t}+\frac{\partial Vh}{\partial x}+\frac{\partial V^2h}{\partial y}=-\frac{1}{2}Rg\frac{\partial C_i h^2}{\partial y}+RgC_{\mathrm{T}}\frac{\partial \eta_{\mathrm{T}}}{\partial y}$$
$$-c_{\mathrm{f}}V\sqrt{U^2+V^2}+\nu_{\mathrm{t}}\left(\frac{\partial^2 Uh}{\partial x^2}+\frac{\partial^2 Vh}{\partial y^2}\right) \tag{A4}$$

$$\frac{\partial Kh}{\partial t}+\frac{\partial UKh}{\partial x}+\frac{\partial VKh}{\partial y}=\left\{c_{\mathrm{f}}+\frac{1}{2}(e_{\mathrm{w}}-d_{\mathrm{w}})\right\}(U^2+V^2)^{\frac{3}{2}}-\epsilon_0 h-Rgw_{si}C_{\mathrm{T}}h$$
$$-\frac{1}{2}RgC_{\mathrm{T}}h(e_{\mathrm{w}}-d_{\mathrm{w}})\sqrt{U^2-V^2}-\frac{1}{2}Rghw_{si}(e_{si}-r_0C_{\mathrm{T}}) \tag{A5}$$

Here, x and y represent the bed-attached horizontal Cartesian coordinates, respectively, and t represents time. The flow thickness is denoted by h. The parameters C_i and C_{T} denote the layer-averaged suspended sediment concentration in the ith grain-size class and the total suspended sediment concentration, respectively, and U and V are layer-averaged flow velocities of x and y directions, respectively. The layer-averaged turbulent kinetic energy is represented by K. The empirical relationship proposed by Parker et al. (1987) is employed as the coefficient of water entrainment e_{w}, which is expressed as:

$$e_{\mathrm{w}}=\frac{0.075}{\sqrt{1+718R_i^{2.4}}}, \tag{A6}$$

where R_i represents the bulk Richardson number, which is defined as:

$$R_i=\frac{RgC_{\mathrm{T}}h}{U^2+V^2}. \tag{A7}$$

Here, the submerged specific density of sediment particles $R=(\rho_{\mathrm{s}}/\rho_{\mathrm{f}}-1)$ and the gravitational acceleration are set to 1.65 and 9.81 m/s^2, respectively. The water detrainment rate d_{w} was calculated as a weighted average of the settling velocities of each grain-size class, using the layer-averaged suspended sediment concentration C_i as the weighting factor:

$$d_{\mathrm{w}} = \gamma \sum_i w_{si} C_i \,, \tag{A8}$$

where γ is the coefficient of the water detrainment rate, set to 3.05 (Salinas et al. 2019), and w_{si} denotes the settling velocity of sediment particles in the ith grain-size class, calculated using the empirical relationship proposed by Ferguson and Church (2004):

$$w_{si} = \frac{RgD_i^2}{X_1 \nu + (0.75 X_2 R g D_i^3)^{0.5}} . \tag{A9}$$

The kinematic viscosity of water, ν, was set to 1.0×10^{-6} m^2/s, corresponding to its value at 20 °C (Lemmon and Harvey 2023). The coefficients X_1 and X_2 were set to 18.0 and 1.0, respectively (Ferguson and Church 2004). The dimensionless sediment entrainment coefficient for the ith grain-size class, e_{si}, is given by the following empirical relationship (Kostic and Parker 2006):

$$e_{si} = p \frac{aZ^5}{1 + \frac{1}{0.3} Z^5} , \tag{A10}$$

$$Z = \alpha_1 \frac{u_*}{w_{si}} Re_{\mathrm{p}i}^{\alpha_2} , \tag{A11}$$

$$(\alpha_1, \alpha_2) = \begin{cases} (0.586, 1.23) & Re_{\mathrm{p}i} \leq 2.36 \\ (1.0, 0.6) & Re_{\mathrm{p}i} > 2.36 \end{cases} , \tag{A12}$$

where $a = 1.3 \times 10^{-7}$. The coefficient p represents the strength of the bed sediment and was set to 0.1 in this study. The bed shear velocity u_* is related to the turbulent kinetic energy K as follows:

$$u_* = \sqrt{\alpha K} = \sqrt{c_{\mathrm{f}}} (U^2 + V^2), \tag{A13}$$

where the basal friction coefficient c_{f} and α were taken as 0.004 (Kostic and Parker 2006; Fujishima and Naruse 2026) and 0.6 (Salinas et al. 2019), respectively. The parameter r_0, representing the ratio of the near-bed concentration to the layer-averaged concentration, was set to 2.0 (Kostic and Parker 2006). The particle Reynolds number $Re_{\mathrm{p}i}$ is defined as

$$Re_{\mathrm{p}i} = \frac{\sqrt{RgD_{\mathrm{s}i}}D_{\mathrm{s}i}}{\nu}. \tag{A14}$$

The parameter ν_{t} is the horizontal eddy viscosity, which is expressed using the following empirical formulation:

$$\nu_{\mathrm{t}} = \frac{1}{6}\kappa u_* h, \tag{A15}$$

where κ is the von Kármán constant and was set to 0.4. The mean dissipation rate of the layer-averaged turbulent kinetic energy, ϵ_0, is given by:

$$\epsilon_0 = \beta\frac{K^{1.5}}{h}, \tag{A16}$$

where

$$\beta = \frac{\alpha^{1.5}}{\sqrt{c_{\mathrm{f}}}}. \tag{A17}$$

Equation A17 is based on the Equation 29 in Fujishima and Naruse (2026).

The sediment mass conservation at the bed and in the active layer take the following forms:

$$\frac{\partial \eta_i}{\partial t} = \frac{w_{\mathrm{s}i}(r_0 C_i - F_i e_{\mathrm{s}i})}{1-\lambda_{\mathrm{p}}}, \tag{A18}$$

$$\frac{\partial \eta_{\mathrm{T}}}{\partial t} = \sum_i \frac{\partial \eta_i}{\partial t}, \tag{A19}$$

$$\frac{\partial F_i}{\partial t} + \frac{F_i}{L_{\mathrm{a}}}\frac{\partial \eta_{\mathrm{T}}}{\partial t} = \frac{w_{\mathrm{s}i}}{L_{\mathrm{a}}\left(1-\lambda_{\mathrm{p}}\right)}(r_0 C_i - F_i e_{\mathrm{s}i}). \tag{A20}$$

Here, the total bed thickness and the sediment volume per unit area of ith grain-size class are denoted by η_{T} and η_i, respectively. The parameter F_i represents the volume fraction of ith grain-size class in the active layer. The porosity of the bed sediment, λ_{p}, was set to 0.4, and the thickness of the active layer, L_{a}, was assumed to be constant at 0.01 m (Cai 2022).

Numerical Scheme

The forward model was implemented using the open-source software *turb2d* (Naruse 2020), which employs the CIP-CUP method as its numerical scheme (Yabe and Wang 1991). The advection and pressure terms of the governing equations are solved using the CIP method and an implicit method, respectively, whereas the non-advection terms, and the sediment mass conservation equations of the bed and the active layer are solved using the semi-implicit Euler method. In addition, the model employs the artificial viscosity (Jameson et al. 1981; Ogata and Yabe 1999), and the wet-dry boundary treatment proposed by Yang et al. (2016).

The time step was determined to satisfy the Courant-Friedrichs-Lewy (CFL) condition as follows (Gunawan 2015):

$$\Delta t = \frac{c\Delta \mathrm{x}}{\max\left(|U| + \sqrt{RgC_{\mathrm{T}}h},\ |V| + \sqrt{RgC_{\mathrm{T}}h},\ 1\right)}, \tag{A21}$$

where Δt and Δx are the time step and grid spacing, respectively. The parameter c denotes the Courant number, which is typically set to a value less than unity to ensure numerical stability. In this study, c was set to 0.4.

APPENDIX B: ARCHITECTURE OF DNN-BASED INVERSE MODEL

The inverse models were implemented as fully connected deep neural networks (DNNs). The DNN-based inverse models were designed to take sediment volumes per unit area at the sampling points as input and to output the input parameters of the forward model. The input layer had a number of nodes corresponding to the number of sampling points, followed by 4 hidden layers with 4,000 nodes each, and an output layer with a number of nodes corresponding to the number of input parameters in the forward model. The activation function used in both the hidden and the output layer was rectified linear unit (ReLU) (Nair and Hinton 2010). Training was performed to minimize the mean squared error between the true and predicted input parameters, using Adagrad as the optimization method (Duchi et al. 2011) with a learning rate of 0.01. In addition, to prevent overfitting, dropout was applied to the hidden layers, and 50% of the nodes in the hidden layers were randomly deactivated during training. The training was conducted for 10,000 epochs with a batch size of 64, and the training datasets were split into an 80% training set and a 20% validation set.

APPENDIX C: EFFECT OF SAMPLING WINDOW LOCATION

To investigate the effect of sampling window location on the inversion, inverse analyses were performed using three different sampling window configurations. The effect of sampling point location was examined by fixing the number of sampling points at 25 and dividing the basin into three regions: proximal, medial, and distal (Fig. C1). Inverse analyses were then conducted for each sampling window, and the resulting training and validation losses were compared. In this analysis, the inverse model was trained using 6,000 datasets.

The inverse model exhibited the best performance when the sampling window was located in the proximal region (Fig. C2). The training and validation losses were 0.015 and 0.026, respectively, for the proximal sampling window. In the medial region, both losses were higher, at 0.025 and 0.034, respectively. For the distal sampling window, the training and validation losses were 0.026 and 0.031, respectively, which were comparable to those obtained for the medial region.

REFERENCES

Cai, Z., 2022, Reconstructing the Behavior of Turbidity Currents From Turbidites-Reference to Anno Formation and Japan Trench [Ph.D. Thesis]: Kyoto University, 162 p., doi:https://doi.org/10.14989/doctor.k24174.

Duchi, J., Hazan, E., and Singer, Y., 2011, Adaptive Subgradient Methods for Online Learning and Stochastic Optimization: Journal of Machine Learning Research, v. 12, p. 2121–2159.

Ferguson, R.I., and Church, M., 2004, A Simple Universal Equation for Grain Settling Velocity: Journal of Sedimentary Research, v. 74, p. 933–937, doi:10.1306/051204740933.

Fujishima, S., and Naruse, H., 2026, Experimental Verification of a Two-Dimensional Inverse Method for Turbidity Currents Using a Deep Neural Network: Journal of Geophysical Research: Machine Learning and Computation, v. 3, p. e2025JH000952, doi:10.1029/2025JH000952.

Gunawan, H.P., 2015, Numerical simulation of shallow water equations and related models [Ph.D Thesis]: Université Paris-Est; Institut teknologi Bandung, 140 p.

Jameson, A., Schmidt, W., and Turkel, E., 1981, Numerical solution of the Euler equations by finite volume methods using Runge Kutta time stepping schemes: 14th Fluid and Plasma Dynamics Conference, AIAA Meeting Paper, doi:10.2514/6.1981-1259.

Kostic, S., and Parker, G., 2006, The response of turbidity currents to a canyon–fan transition: internal hydraulic jumps and depositional signatures: Journal of Hydraulic Research, v. 44, p. 631–653, doi:10.1080/00221686.2006.9521713.

Lemmon, E.W., and Harvey, A.H., 2023, Thermophysical properties of water and steam, *in* Rumble, J.R. ed., CRC Handbook of Chemistry and Physics: CRC Press.

Nair, V., and Hinton, G.E., 2010, Rectified Linear Units Improve Restricted Boltzmann Machines: The 27th international conference on machine learning, Proceedings of the 27th international conference on machine learning, p. 807–814.

Naruse, H., 2020, Numerical simulation of turbidity current by open source software “turb2d”: Journal of the Sedimentological Society of Japan, v. 78, p. 54, doi:10.4096/jssj.78.54.

Ogata, Y., and Yabe, T., 1999, Shock capturing with improved numerical viscosity in primitive Euler representation: Computer Physics Communications, v. 119, p. 179–193, doi:10.1016/s0010-4655(99)00188-5.

Parker, G., Fukushima, Y., and Pantin, H.M., 1986, Self-accelerating turbidity currents: Journal of Fluid Mechanics, v. 171, p. 145–181, doi:10.1017/S0022112086001404.

Parker, G., Garcia, M., Fukushima, Y., and Yu, W., 1987, Experiments on turbidity currents over an erodible bed: Journal of Hydraulic Research, v. 25, p. 123–147, doi:10.1080/00221688709499292.

Salinas, J.S., Cantero, M.I., Shringarpure, M., and Balachandar, S., 2019, Properties of the Body of a Turbidity Current at Near-Normal Conditions: 2. Effect of Settling: Journal of Geophysical Research: Oceans, v. 124, p. 8017–8035, doi:10.1029/2019JC015335.

Yabe, T., and Wang, P.-Y., 1991, Unified Numerical Procedure for Compressible and Incompressible Fluid: Journal of The Physical Society of Japan, v. 60, p. 2105–2108, doi:https://doi.org/10.1143/JPSJ.60.2105.

Yang H., Lu M., and Kumakura T., 2016, A study on the water front in shallow water equations: Journal of Japan Society of Civil Engineers, Ser. B1 (Hydraulic Engineering), v. 72, p. I_325–I_330, doi:10.2208/jscejhe.72.i_325.

FIG. C1.--- Sampling windows used to validate the performance of the inverse model.

FIG. C2.--- Comparison of the training and validation losses for sampling windows in the proximal, medial, and distal regions.

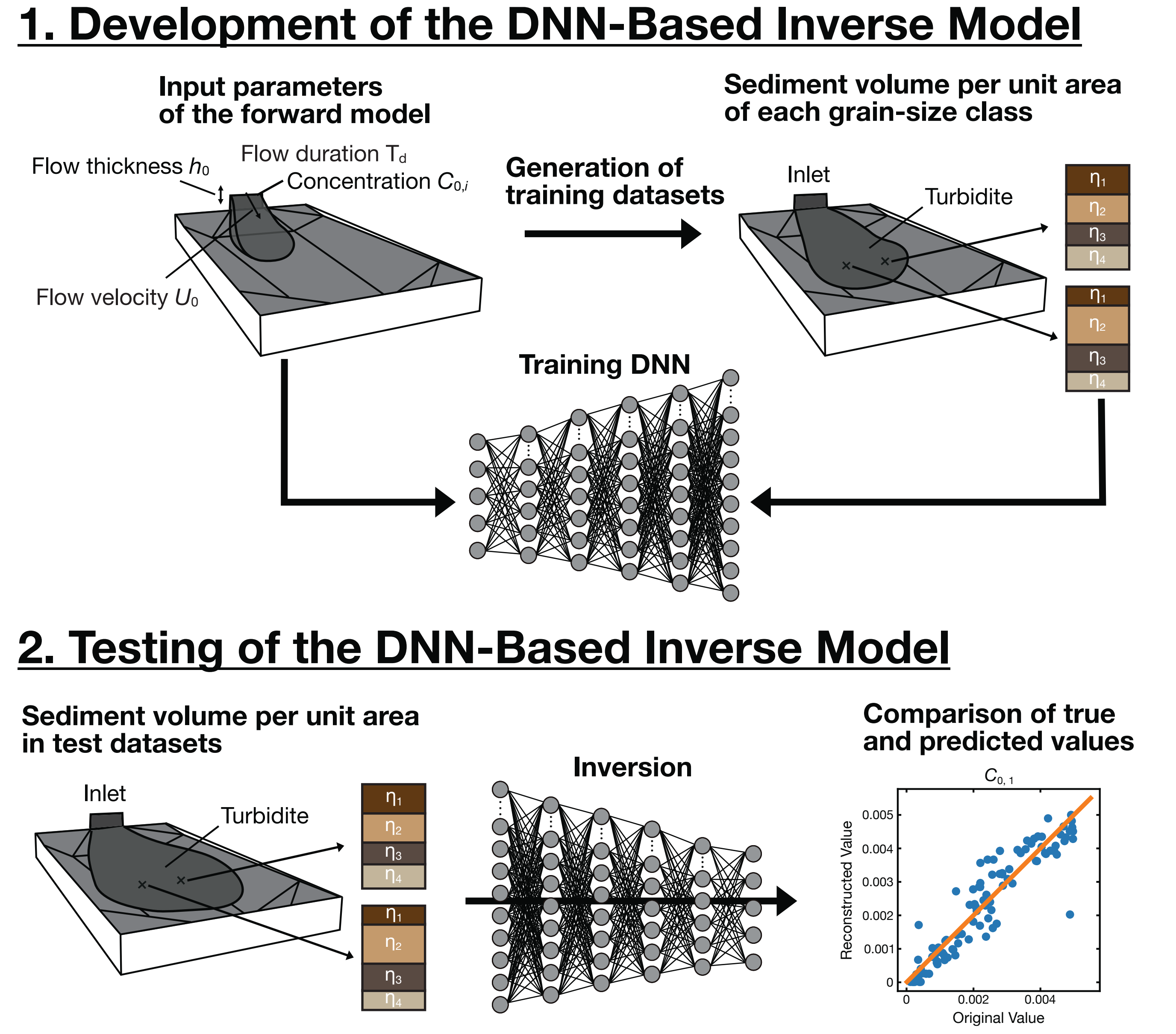
1. Development of the DNN-Based Inverse Model
Input parameters of the forward model
Flow thickness h_0
Flow duration T_d
Concentration $C_{0,i}$
Flow velocity U_0
Generation of training datasets
Sediment volume per unit area of each grain-size class
Inlet
Turbidite
η_1
η_2
η_3
η_4
Training DNN
2. Testing of the DNN-Based Inverse Model
Sediment volume per unit area in test datasets
Inlet
Turbidite
Inversion
Comparison of true and predicted values
$C_{0,1}$
Reconstructed Value
Original Value
0.005
0.004
0.003
0.002
0.001
0
0.002
0.004

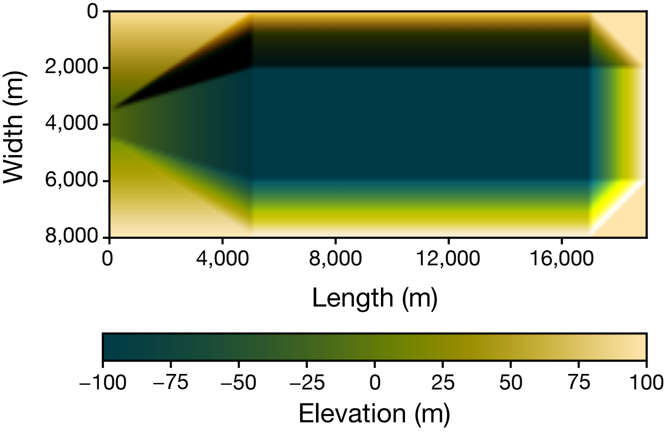

Width (m)
0
2,000
4,000
6,000
8,000
0
4,000
8,000
12,000
16,000
Length (m)
−100
−75
−50
−25
0
25
50
75
100
Elevation (m)

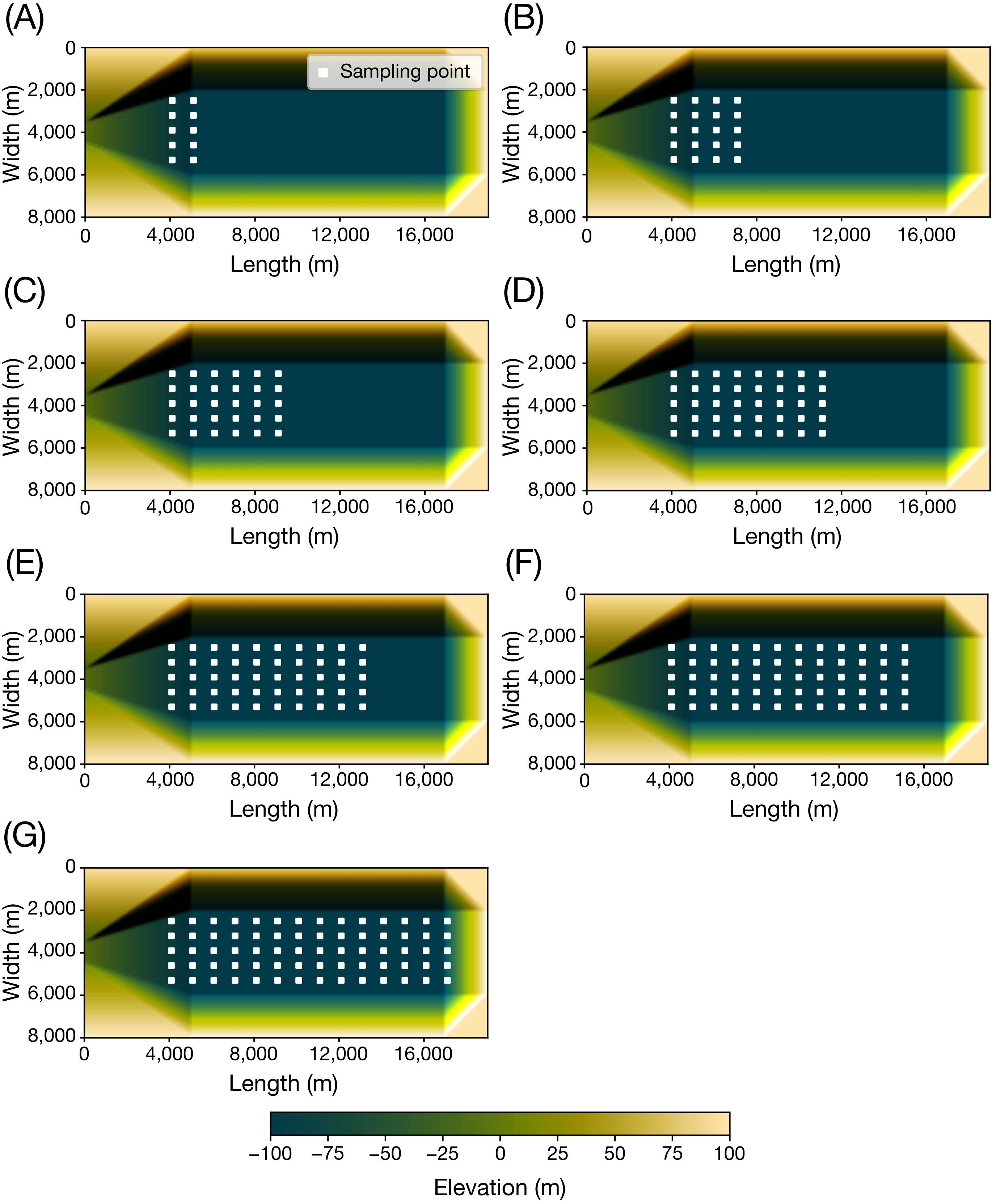
(A)
(B)
(C)
(D)
(E)
(F)
(G)
Sampling point
Width (m)
Length (m)
0
2,000
4,000
6,000
8,000
0
4,000
8,000
12,000
16,000
−100
−75
−50
−25
0
25
50
75
100
Elevation (m)

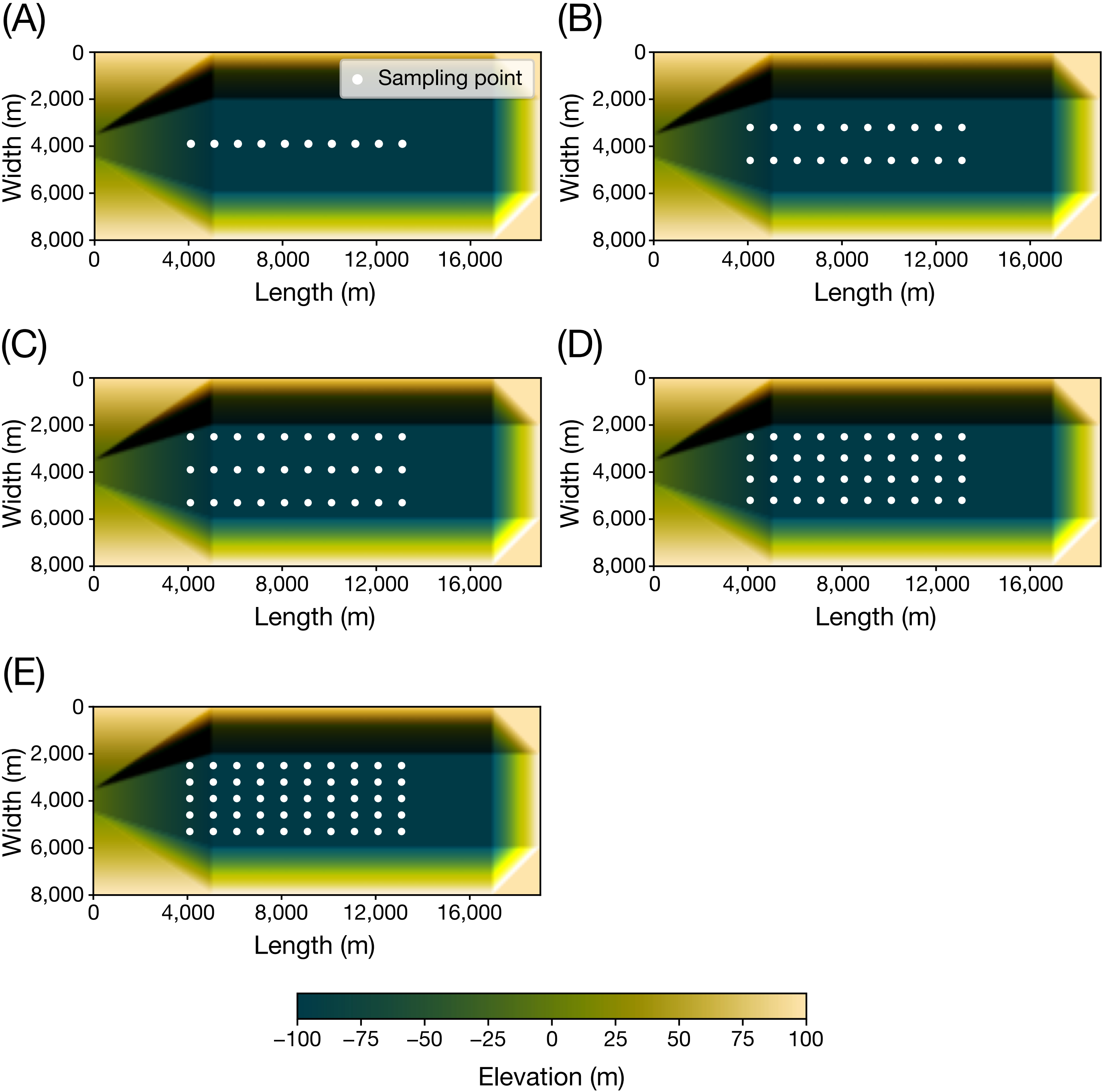
(A)
(B)
(C)
(D)
(E)
Sampling point
Width (m)
Length (m)
0
2,000
4,000
6,000
8,000
0
4,000
8,000
12,000
16,000
−100
−75
−50
−25
0
25
50
75
100
Elevation (m)

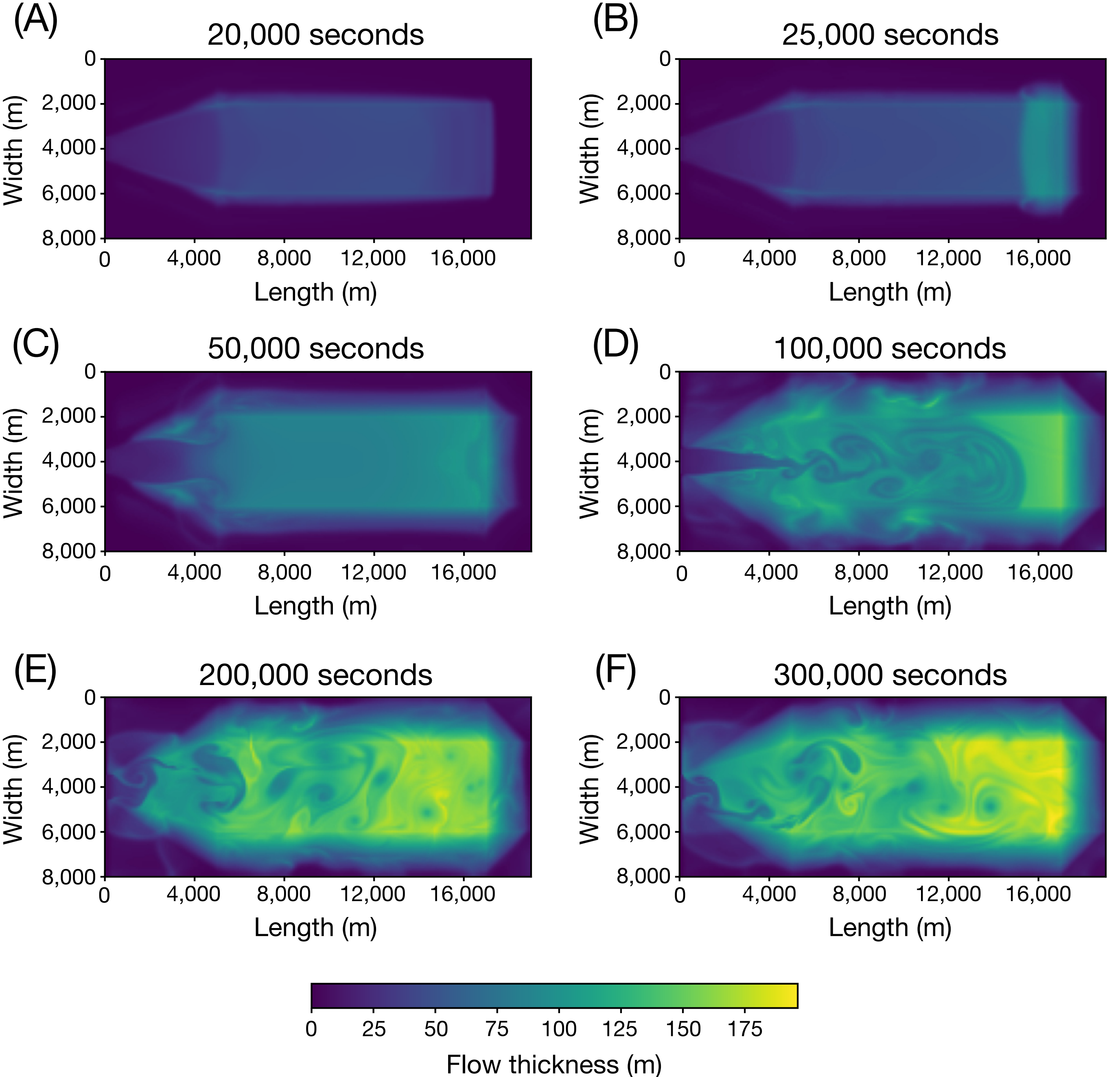

(A)
20,000 seconds
(B)
25,000 seconds
(C)
50,000 seconds
(D)
100,000 seconds
(E)
200,000 seconds
(F)
300,000 seconds
Width (m)
0
2,000
4,000
6,000
8,000
Length (m)
0
4,000
8,000
12,000
16,000
0
25
50
75
100
125
150
175
Flow thickness (m)

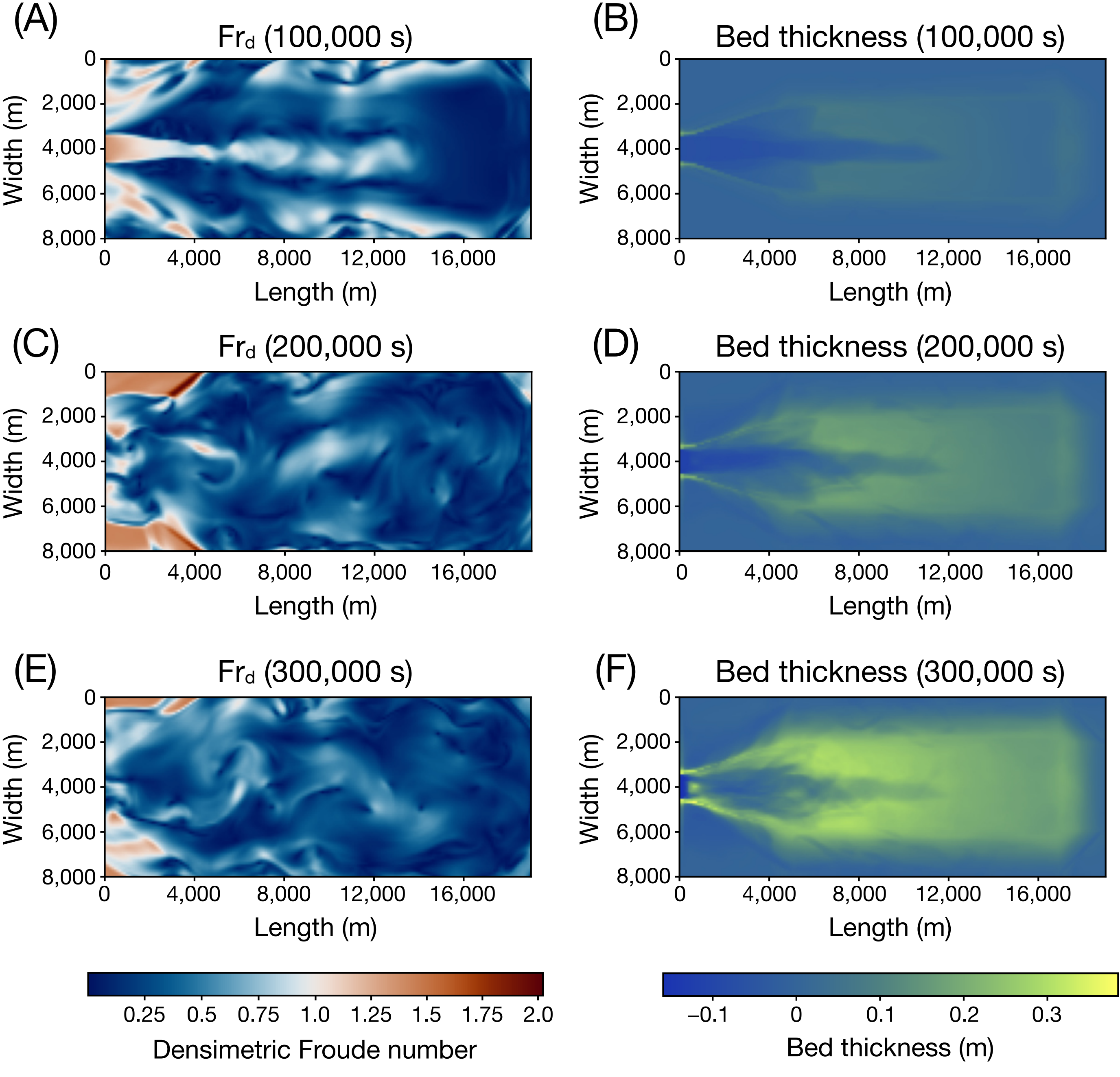
(A)
Frd (100,000 s)
(B)
Bed thickness (100,000 s)
(C)
Frd (200,000 s)
(D)
Bed thickness (200,000 s)
(E)
Frd (300,000 s)
(F)
Bed thickness (300,000 s)
Width (m)
0
2,000
4,000
6,000
8,000
Length (m)
0
4,000
8,000
12,000
16,000
0.25
0.5
0.75
1.0
1.25
1.5
1.75
2.0
Densimetric Froude number
−0.1
0
0.1
0.2
0.3
Bed thickness (m)

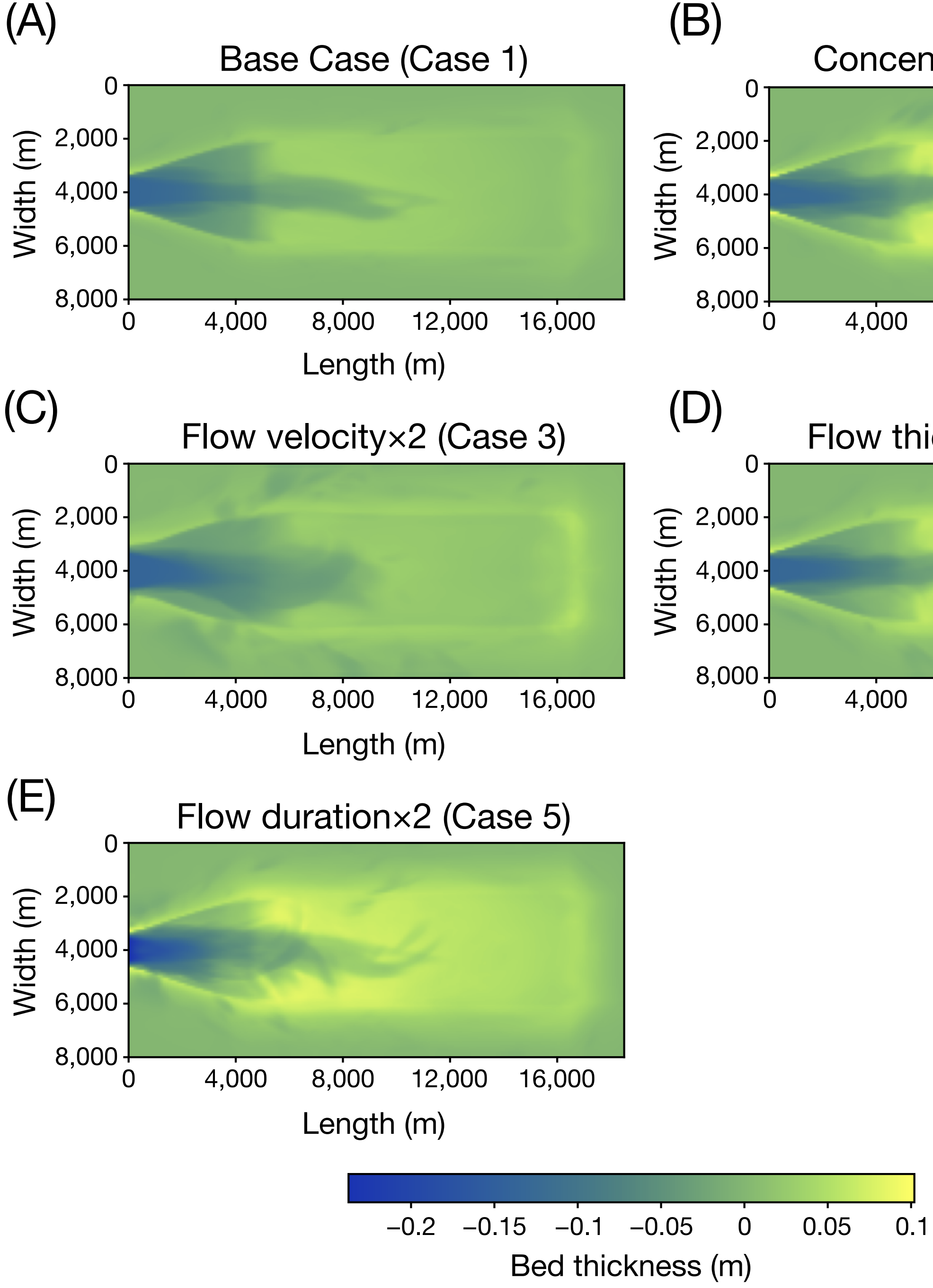
(A)
Base Case (Case 1)
(B)
Concentration×2 (Case 2)
(C)
Flow velocity×2 (Case 3)
(D)
Flow thickness×2 (Case 4)
(E)
Flow duration×2 (Case 5)
Width (m)
Length (m)
0
2,000
4,000
6,000
8,000
12,000
16,000
−0.2
−0.15
−0.1
−0.05
0.05
0.1
Bed thickness (m)

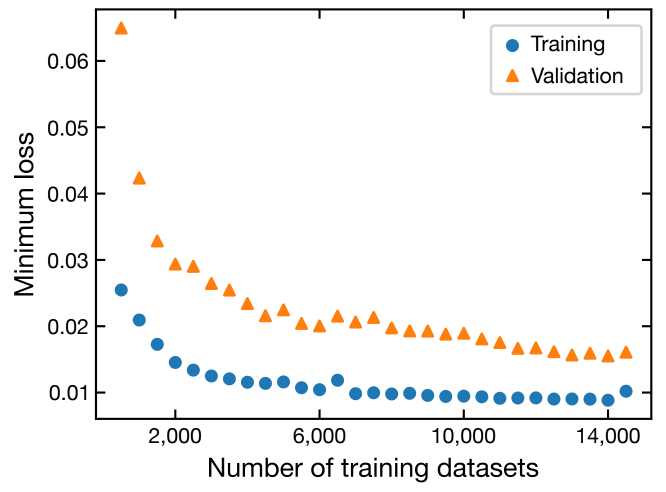
Training
Validation
0.06
0.05
0.04
0.03
0.02
0.01
Minimum loss
2,000
6,000
10,000
14,000
Number of training datasets

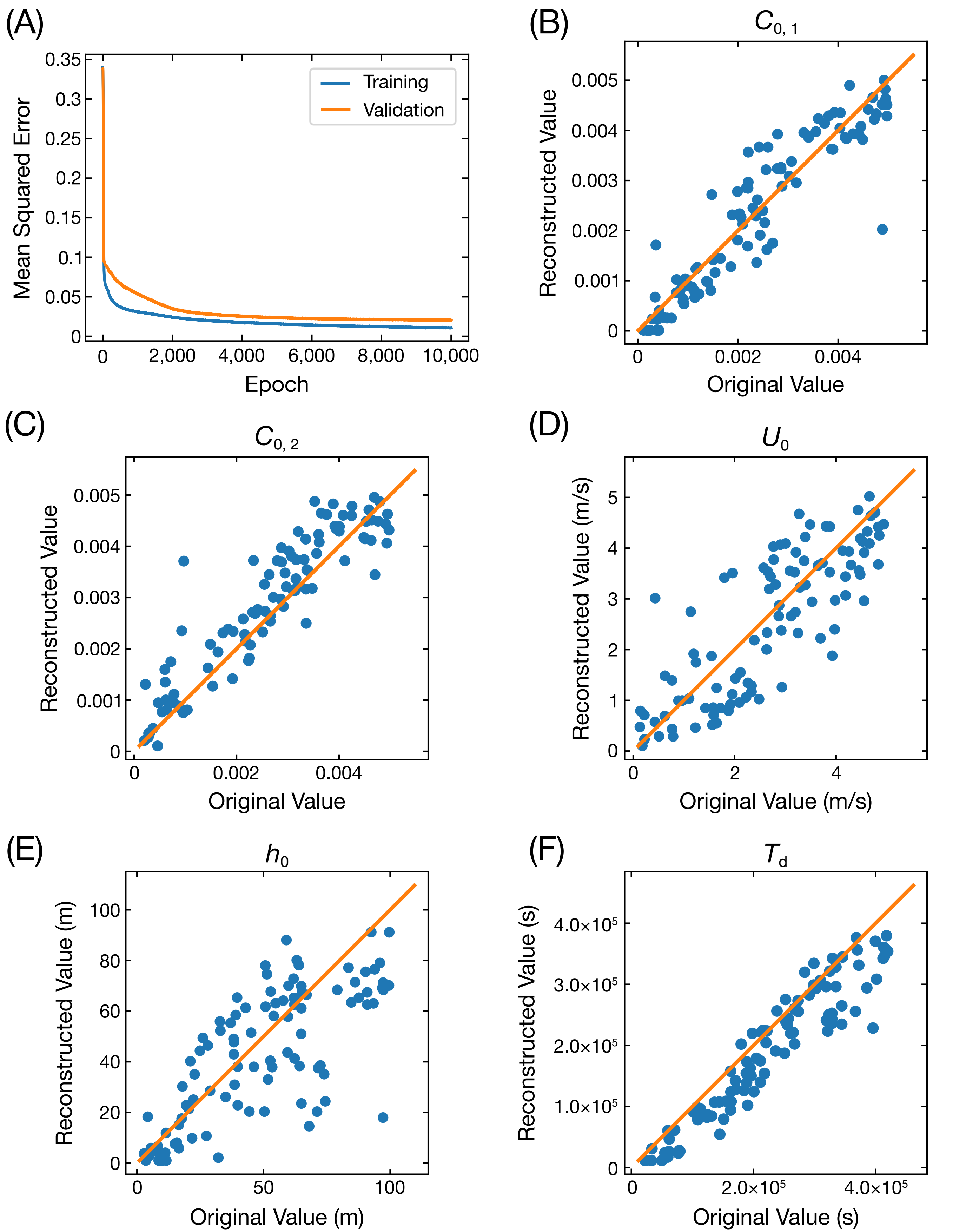

(A)
Mean Squared Error
Epoch
Training
Validation
(B)
$C_{0,1}$
Reconstructed Value
Original Value
(C)
$C_{0,2}$
Reconstructed Value
Original Value
(D)
U_0
Reconstructed Value (m/s)
Original Value (m/s)
(E)
h_0
Reconstructed Value (m)
Original Value (m)
(F)
T_d
Reconstructed Value (s)
Original Value (s)

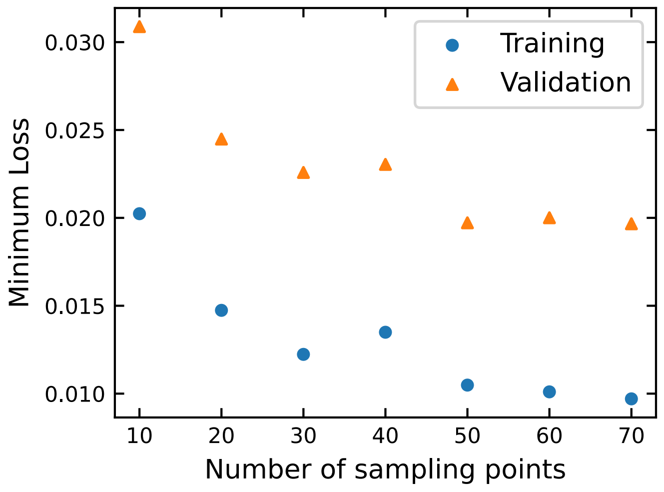

Training
Validation
Minimum Loss
0.030
0.025
0.020
0.015
0.010
10
20
30
40
50
60
70
Number of sampling points

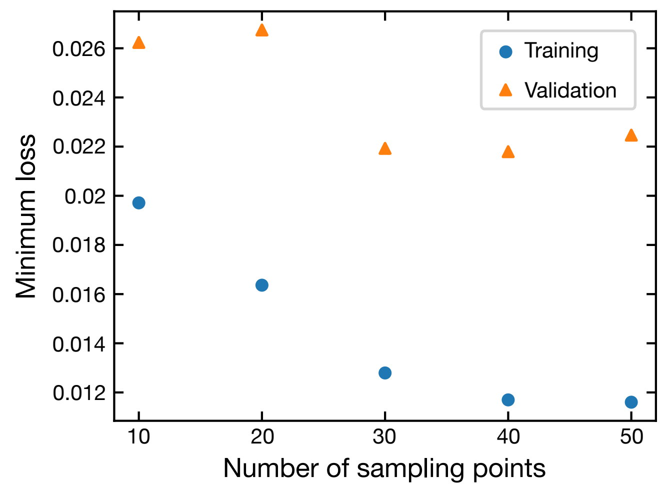

Training
Validation
Minimum loss
0.026
0.024
0.022
0.02
0.018
0.016
0.014
0.012
10
20
30
40
50
Number of sampling points

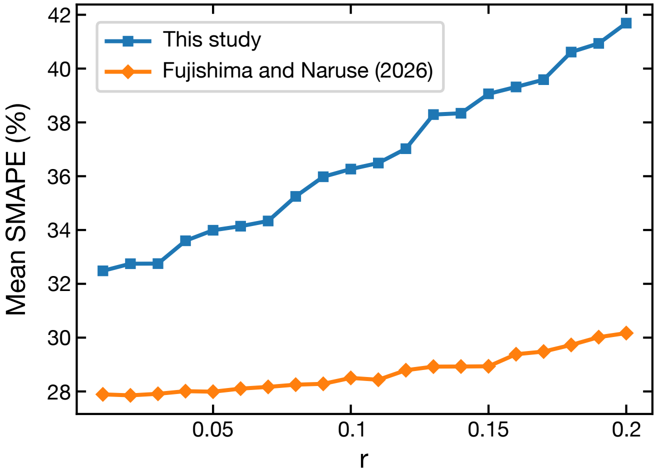
This study
Fujishima and Naruse (2026)
Mean SMAPE (%)
42
40
38
36
34
32
30
28
0.05
0.1
0.15
0.2
r

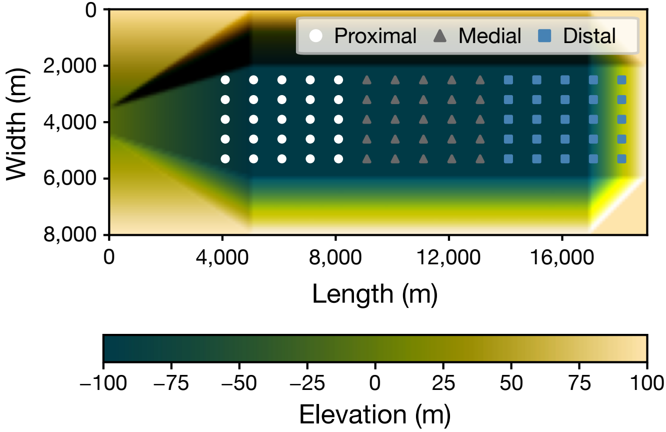
Proximal
Medial
Distal
Width (m)
0
2,000
4,000
6,000
8,000
0
4,000
8,000
12,000
16,000
Length (m)
−100
−75
−50
−25
0
25
50
75
100
Elevation (m)

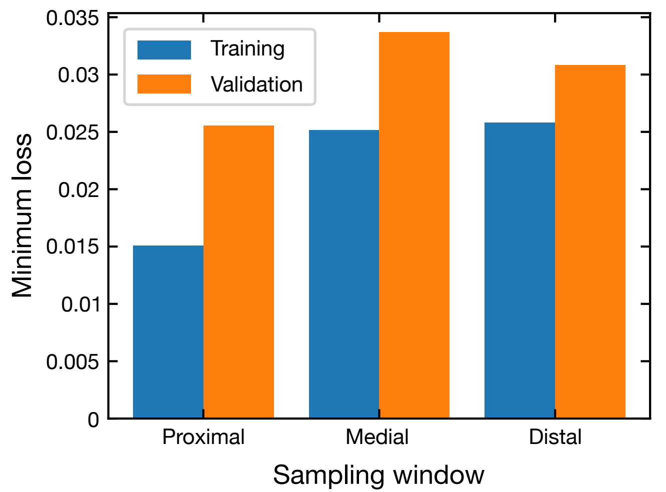

Training
Validation
Minimum loss
0.035
0.03
0.025
0.02
0.015
0.01
0.005
0
Proximal
Medial
Distal
Sampling window

TABLE 1. Input parameters for the forward model used in the sensitivity test.

	Case 1	Case 2	Case 3	Case 4	Case 5
$C_{0,1}$ (20 μm)	0.001	0.002	0.001	0.001	0.001
$C_{0,2}$ (3 μm)	0.001	0.002	0.001	0.001	0.001
U_0 (m/s)	2.0	2.0	4.0	2.0	2.0
h_0 (m)	4.0	4.0	4.0	8.0	4.0
T_d (s)	200,000	200,000	200,000	200,000	400,000

TABLE 2. Ranges of input parameters for the forward model used to generate the training datasets.

	Min Value	Max Value
$C_{0,i}$	0.00001	0.005
U_0 (m/s)	0.1	5.0
h_0 (m)	1.0	100.0
T_d (s)	1800	432,000

TABLE 3. SMAPE, RMSE, and bias for predicted values obtained by inversion on the test datasets.

	$C_{0,1}$ (20 μm)	$C_{0,2}$ (3 μm)	U_0	h_0	T_d
SMAPE	32.0%	21.9%	36.8%	45.0%	27.4%
RMSE	0.000575	0.000618	0.855 m/s	20.5 m	50,290 s
bias	−0.0000274	0.000259	−0.152 m/s	−6.09 m	−35,674 s